Book Chapter

Surface Study of Fe$_3$O$_4$ Nanoparticles Functionalized With Biocompatible Adsorbed Molecules

Beata Lesiak[1]*, N Rangam[1]*, P Jiricek[2], I Gordeev[2], J Tóth[3], L Kövér[3], M Mohai[4] and P Borowicz[1]

[1]Institute of Physical Chemistry, Polish Academy of Sciences, Poland
[2]Institute of Physics, Academy of Sciences of the Czech Republic, Czechia
[3]Institute for Nuclear Research, Hungarian Academy of Sciences, Hungary
[4]Research Centre for Natural Sciences, Institute of Materials and Environmental Chemistry, Hungarian Academy of Sciences, Hungary

*Corresponding Authors: Beata Lesiak, Institute of Physical Chemistry, Polish Academy of Sciences, Warsaw, Poland

N Rangam, Institute of Physical Chemistry, Polish Academy of Sciences, Warsaw, Poland

Published **August 06, 2021**

How to cite this book chapter: Beata Lesiak, N Rangam, P Jiricek, I Gordeev, J Tóth, L Kövér, M Mohai, P Borowicz. Surface Study of Fe$_3$O$_4$ Nanoparticles Functionalized With Biocompatible Adsorbed Molecules. In: VSR Rajasekhar

Conflict of Interest Statement: The authors declare that the research was conducted in the absence of any commercial or financial relationship that could be construed as a potential conflict of interest.

Abstract

Surfaces of iron oxide of ferrimagnetic magnetite (Fe$_3$O$_4$) nanoparticles (MNPs) prepared by Massart's method and their functionalized form (f-MNPs) with succinic acid, L-arginine,

oxalic acid, citric acid and glutamic acid were studied by DLS, FTIR, UV-vis, TGA/DSC, X-ray photoelectron spectroscopy (XPS) and reflection electron energy loss spectroscopy (REELS).

The XPS analysis of elements and their chemical states at the surface of MNPs and f-MNPs revealed differences in chemical bonding of atoms, content of carbon-oxygen groups, iron oxide forms, iron oxide magnetic properties, adsorbed molecules surface coverage and overlayer thickness, whereas the Auger parameters (derived from XPS and Auger spectra), elastic and inelastic scattering probabilities of electrons on atoms and valence band electrons (derived from REELS spectra) indicated modification of surface charge redistribution, electronic and optical properties. These modified properties of f-MNPs influenced their biological properties.

The surfaces biocompatible for L929 cells showed various cytotoxicity for HeLa cells (10.8-5.3% of cell death), the highest for MNPs functionalized with oxalic acid. The samples exhibiting the largest efficiency possessed smaller surface coverage and thickness of adsorbed molecules layers, the highest content of oxygen and carbon-oxygen functionalizing groups, the highest ratio of lattice O^{2-} and OH^- to C sp^2 hybridizations on MNPs surface, the highest ratio of adsorbed O^- and OH^- to C sp^2 hybridizations on adsorbed molecule layers, the closest electronic and optical properties to Fe_3O_4 and the lowest degree of admolecule polymerization. This high cytotoxicity was attributed to interaction of surface with cells, where increased content of oxygen groups, adsorbed O^- and OH^- may play a role of additional adsorption and catalytic sites and a large content of adsorbed molecule layers carboxylic groups facilitating Fenton reaction kinetics leading to cells damage.

Keywords

Ferrimagnetic Magnetite (Fe_3O_4) Magnetic Nanoparticles; Biocompatible Acid Functionalization; DLS; FTIR-S; TGA/DSC; XPS; REELS; HeLa Cells

Introduction

The iron oxide nanoparticles like i.e. ferrimagnetic maghemite (γ-Fe$_2$O$_3$) with Fe^{3+} vacancies and ferrimagnetic magnetite (Fe$_3$O$_4$ $\equiv$ FeO$\bullet$Fe$_2$O$_3$) with Fe^{2+} and Fe^{3+} vacancies have been already applied in the field of medicine due to their biocompatibility, biodegradability and possibility to tailor magnetic behaviour [1], where the change of nanoparticle size, morphology, agglomeration, magnetic and electronic properties influences the biological effect [2]. Although, magnetic targeting iron nanoparticles serve as platforms for attaching drugs like e.g. doxorubicin (DOX), they were also applied in a tumor therapy, which resulted in a hyperthermia and oxidative stress leading to tumor cell damage [1,3,4]. Enhancement of antitumor effect was obtained by functionalization of nanoparticles by a conventional DOX drug [2,3] and/or doping with rare metals [4]. Additional functionalization of iron nanoparticles may lead to enhancement of their biocompatibility, colloidal stability and enlargement of number of groups, through which the required antitumor effect can be obtained.

The cytotoxicity of Fe$_3$O$_4$ MNPs coated with a wide variety of biocompatible admolecules has been recently extensively studied [5-13]. These several studies showed that cytotoxicity depends on the type of the investigated cells, type of biocompatible adlayer on MNPs, MNPs size, concentration of MNPs, pH of solution and time of incubation. The functionalization of MNPs with biocompatible molecules like polyethylene glycol, pluronic acid and others providing a better biocompatibility may also affect the cytotoxicity due to modification of physical and chemical properties of the material, its interaction with biological cells and ability of forming reactive oxygen species (ROS). The coating of Fe$_3$O$_4$ MNPs may provide a positive charge, which facilitates interaction of a specimen with negatively charged cell membrane [8]. For the concentration range of 0.012-0.1 mg mL^{-1} the generation of ROS by Fe$_3$O$_4$ nanoparticles was found to be smaller in comparison to Pt and PEGylated mesoporous iron-platinum-iron(II,III) (FePt-Fe$_3$O$_4$) nanoparticles [9]. Recently, it has been reported that Fe$_3$O$_4$ MNPs exhibited no cytotoxicity for HeLa cells during incubation

time from 24h to 72 h, whereas coated MNPs showed the cytotoxicity after 72 h [5]. No effect of Fe_3O_4 MNPs on cytotoxicity for HeLa cells was observed for incubation time of 24 h elsewhere [10-13].

Functionalized nanoparticles of Fe_3O_4 iron oxide prepared by Massart's method [14,15] (f-MNPs) using functionalization with succinic acid ((CH_2)$_2$(CO_2H)$_2$), L-arginine ($C_6H_{14}N_4$), oxalic acid ($C_2H_2O_4$), citric acid ($C_6H_8O_7$) and glutamic acid ($C_5H_9O_4N$) showed similar biocompatibility on fibroblasts [3]. Their average efficiency on HeLa cell treatment (% of HeLa cell deaths) in f-MNPs concentration range of 3.125-100 $\mu g\ mL^{-1}$ and incubation time of 24 h decreased in the following order: 10.8 % (oxalic acid), 10.7 (succinic acid), 9.2 % (glutamic acid), 7.5 % (citric acid) and 5.3 % (L-arginine) [3]. The respective f-MNPs loaded with DOX showed about 6 times higher efficiency on HeLa cell therapy decreasing in different order, i.e. 64.2 % (oxalic acid), 55.2 % (L-arginine), 42.8 % (glutamic acid), 42.2 % (succinic acid) and 32.7 % (citric acid), what is attributed to DOX adsorption and modified surface properties [3].

The reason for different cytotoxicity of Fe_3O_4 MNPs functionalized with oxalic, succinic, glutamic acids and L-arginine for HeLa cells was investigated by X-ray photoelectron spectroscopy (XPS), X-ray excited Auger electron spectroscopy (XAES) and reflected electron loss spectroscopy (REELS) revealing the chemical groups at the surface and modification of surface electronic properties. These studies were supported by dynamic light scattering (DLS), Fourier transform infrared spectroscopy (FTIR-S), UV-vis, thermogravimetric analysis (TGA) and differential scanning calorimetry (DSC).

Experimental
Samples

Details on synthesis of nanoparticles of iron oxide (Fe_3O_4) by Massart's method (MNPs) [14,15] and their functionalization at temperature of 70 ^{o}C-80 ^{o}C at pH ca. 6-7 for 30 minutes with succinic acid ((CH_2)$_2$(CO_2H)$_2$), L-arginine ($C_6H_{14}N_4$), oxalic acid ($C_2H_2O_4$), citric acid ($C_6H_8O_7$) and glutamic acid ($C_5H_9O_4N$)

(samples denoted as I, II, III, IV and V, respectively) were described elsewhere [3]. The structural formulae of functionalizing adsorbed molecules are shown in **Figure S1**. The prepared samples' (Fe_3O_4 MNPs and Fe_3O_4 f-MNPs I-V) chemical, structural and magnetic properties were characterized previously by energy dispersive X-ray spectroscopy (EDX), scanning electron microscopy (SEM), transmission electron microscopy (TEM), X-ray diffraction (XRD) and vibrating sample magnetometer [3].

DLS, FTIR-S, UV-vis, TGA/DSC Apparatuses

The DLS measurements were carried out using Brookhaven Instruments Particle Size Analyser 90+ to determine nanoparticles hydrodynamic diameter (D_H), polydispersity index (PDI) and Zeta potential. The measurements were performed in a water suspension of concentration of 0.01 mg mL^{-1} at pH ca. 6.

The FTIR spectra were recorded in Fourier spectrophotometer Vertex 80 V (Bruker Inc., USA) in a configuration of attenuated total reflectance (ATR) at the pressure below 5 hPa, what reduces negative factors like carbon dioxide and water. In order to obtain a high spectral resolution and signal-to-noise ratio the following apparatus conditions were applied during the measurement: spectral resolution of 2 cm^{-1} and a number of scans of 1024.

The UV-vis spectra were recorded in deionized water solution by Shimazu UV-2401 spectrophotometer.

The TGS/DSC data was recorded using Mettler Toledo TGA/DSC 3+ apparatus in nitrogen flow in a temperature range from room temperature (RT) to 800 ^{o}C at the heating rate of 10 ^{o}C min^{-1}.

XPS Spectrometer

The XPS spectra of Fe_3O_4 MNPs and Fe_3O_4 f-MNPs I-V were measured in an ultra-high vacuum (UHV) AXIS Supra photoelectron spectrometer (Kratos Analytical, UK). The

incidence angle of the monochrome Al K_α radiation (1 mm^2 irradiation area, 300 x 700 μm analyzed area) was set to 54.4° and the photoelectron emission angle was α_{out}=0°, with respect to the surface normal. The hemispherical electron energy analyzer operated in the constant analyzer energy (CAE) mode at analyzer pass energy of E_p=80 eV (survey spectra) and E_p=10 eV (high resolution detailed spectra). The data acquisition was performed using ESCApe Kratos software. The samples were investigated without any UHV pretreatment. The binding energies (BE) of all the spectra were referenced to BE of 284.4 eV of C 1s line.

The REELS measurements proceeded in an ultra-high-vacuum (UHV) chamber using the ESA-31 electron spectrometer (home-made) [16]. The spectrometer is equipped with a hemispherical electron energy analyzer of high energy resolution, an electron gun (LEG62-VG Microtech), a home-made X-ray excitation source (Al Kα X-rays hν=1486.67 eV) and an Ar$^+$ ion source of AG21 (VG Scientific). The REELS spectra were measured at fixed retardation ratio (FRR) mode using the retardation ratio of k=41. The electron beam parameters were: primary electron energy of 4 keV, the beam current of about 11.5 nA measured with a Faraday cup and the electron incidence and emission angles of 50° and 0° with respect to the surface normal of the specimen, respectively.

Results and Discussion
DLS, FTIR-S, UV-vis and TGA/DSC

The investigated Fe_3O_4 MNPs and Fe_3O_4 f-MNPs I-V exhibit various values of hydrodynamic diameter (D_H), polydispersity index (PDI) and Zeta potential. The values of D_H vary in a range of 217.9-871.2 nm (III < V < I < Fe_3O_4 < IV < II). Larger values of D_H in comparison to SEM values [3] would suggest polymeric coating formed from adsorbed molecules on Fe_3O_4 MNPs. The values of polydispersity are in a range of 0.039-0.853 (IV < I < Fe_3O_4 < II < V < III) indicating different agglomeration/aggregation of nanoparticles in a solution. The value of Zeta potential at pH ca. 6 is a range of -0.53-0.83 mV (I < II < IV < V < Fe_3O_4 < III).

The ATR-FTIR spectra of Fe_3O_4 MNPs and f-MNPs I-V are shown in **Figure 1A**. All spectra show the characteristic peak of iron oxides, i.e. Fe-O at 548 cm^{-1}. The literature reports this peak at 580 cm^{-1} [17-19]. However, these reported data result from measurements in a polar environment of KBr pellet, what may shift the peak position. The spectrum of Fe_3O_4 MNPs exhibits modes typical for organic groups in regions of 760-1800 cm^{-1}, about 2000 cm^{-1} and 2500-3600 cm^{-1}. The spectra of Fe_3O_4 MNPs I-V samples confirm the presence of adsorbed molecules layers. All the spectra were normalized to the intensity of Fe-O peak at 548 cm^{-1} in order to compare the intensity of peaks at different spectra regions for various adsorbed molecules. The FTIR spectra can be divided into the following regions: **760-1180 cm^{-1}**, **1180-1480 cm^{-1}**, **1480-1800 cm^{-1}**, region **about 2000 cm^{-1}**, **2500-3600 cm^{-1}**. In the region of **760-1180 cm^{-1}** C-C stretching (strong) and C-N stretching (medium) exist (Infrared Spectroscopy – MSU Chemistry). This region encloses the complex skeleton modes involving few vibration local modes due to modification of length of the bonds and angles between the bonds. Such vibration modes have been previously observed for L-arginine [20] and glutamic acid [21]. For Fe_3O_4 f-MNPs II and V dominating signal should results from C-C stretching. In the region of **1180-1480 cm^{-1}** the functionalized MNPs modes characteristic for COOH group exist, i.e. stretching C-O mode (medium strong) (Infrared Spectroscopy - MSU Chemistry; Silverstein et al., [22]), bending C-O-H mode (medium) and bending C-H mode [22]. For the investigated admolecules the literature reports symmetric stretching COOH$^-$ mode for succinic acid [23], CH$_3$ symmetric bending mode for L-arginine [20], stretching C-O mode for oxalic acid [24], scissoring C-O-H, CH$_2$, CH$_3$ modes, wagging CH$_2$, CH$_3$ modes for citric acid [25] and different types of bending C-H and stretching C-O modes for glutamic acid [21]. In the region of **1480-1800 cm^{-1}** C=O stretching mode (strong) is dominating (Infrared Spectroscopy - MSU Chemistry; Silverstein et al., [22]). For sample MNPs III this mode is shifted to higher frequencies and among all the samples this mode resembles the structure of COOH group in oxalic acid. For samples MNPs I and IV this mode is shifted to lower frequencies, i.e. to 1550 cm^{-1}. The structure of samples MNPs III is more rigid than structure of samples MNPs I and

MNPs IV. The interaction of COOH groups in f-MNPs III with Fe_3O_4 is weak. This is shown in bending of a mode at about 1705 cm^{-1} typical for COOH group interacting weakly with Fe_3O_4 MNPs. The main mode maximum at about 1645 cm^{-1} is attributed to C=O mode of stronger interaction with MNPs. For samples MNPs I and IV their less rigid structure allows for attraction of all COOH groups to Fe_3O_4, what results in a larger frequency shift of C=O mode to lower values. For samples MNPs II and V the mode in a range of 1490-1705 cm^{-1} there is an overlap of stretching C=O mode (strong) [26] and bending N-H mode (medium/medium-strong) typical for amine and amide [26]. Contribution of bending N-H mode and interaction of COOH with Fe_3O_4 result in a mode position and shape, where for smaller frequencies the slope responsible for bending N-H mode is smaller than for stretching C=O mode. The region at about **2000 cm^{-1}** consists of weak modes responsible for combination and overtones of basic modes. The region of 2500-3600 cm^{-1} encloses stretching O-H modes (strong and wide depending on the environment), stretching C-H modes (generally strong) and stretching N-H mode typical for amine groups (samples MNPs II and V) [26]. Since the intensity of N-H stretching mode in this region is weak the main components are stretching O-H and C-H modes with contributions depending on the sample.

The UV-vis spectra of Fe_3O_4 MNPs (**Figure 1B**) indicate the absorption band between 400-420 nm characteristic for Fe_3O_4 nanoparticles as reported elsewhere [27] and at about 300 nm reported previously for Fe_2O_3 [28]. Less intense absorption bands with intensity decreasing in the order of I > II > III ≈ V > IV and shifted to a smaller wavelengths exhibit Fe_3O_4 f-MNPs I-V samples due to adsorbed molecules. The shift may be attributed to adsorbed molecules, where L-arginine absorption band at 226-278 nm has been reported [20].

The TGA curves (**Figure 1C, Figure S2**) indicate various weight loss for every investigated sample in different temperature regions. The temperature range of 30-150 ^{o}C is characteristic for a loss of residual water and other contaminations, as well as for physically adsorbed molecules. In the temperature range of 150-

600 ^{o}C carboxyl, hydroxyl, carbonyl and nitrogen groups of chemically adsorbed molecules undergo decomposition [5,29-31] contributing to this weight loss, whereas higher temperatures are more characteristic for phase transformations. The weight loss for all the investigated samples in the first range varies from 2.3 % to 5.4 % and is larger for oxalic (5.4 %) and citric (4.6 %) acids indicating either higher surface hydrophilicity and/or physical adsorption. The weight loss in the second region is 2.8 % for Fe_3O_4 MNPs, 8 % and 8.5 % for L-arginine and succinic acid, 10.5 % and 10.9 % for oxalic and glutamic acid and 21.4 % for citric acid. This weight loss between 10.5 % and 21.4 % indicates citric, oxalic and glutamic acids dissolution in Fe_3O_4, where dissolution in oxalic acid was reported elsewhere [32]. Thermal stability decreases in the following order: Fe_3O_4 MNPs > II (f-L-arginine) > I (f-succininc acid) > III (f-oxalic acid) > V (f-glutamic acid) > IV (f-citric acid).

The DSC curves (**Figure 1D, Figure S2**) show endothermic and exothermic peaks indicating respectively heat absorption and release. The endothermic peaks are attributed to phase transitions, reduction and most decomposition reactions, whereas exothermic peaks are related with oxidation, decomposition reactions and crystallization. The first endothermic peaks visible for all the samples at 50.5-71.3 ^{o}C can be attributed to desorption and/or evaporation of water and is related with the weight loss from 1.9 % for Fe_3O_4 MNPs to 5.4 % for f-MNPs I-V. The endothermic peaks in a range of 190–224 ^{o}C can be attributed to desorption and/or decomposition of carboxylic groups and are related with the weight loss of 1.7-15.7 %. This peak maximum temperature shift, i.e. Fe_3O_4 MNPs < I ≈ III < IV ≈ V < II, indicates increasing binding energy between MNPs and carboxylic groups from functionalizing molecules. The other broad exothermic peaks in a range of 320-420 ^{o}C (Fe_3O_4 MNPs < I < V < II < IV) with a weight loss of 1.1-5.7 % (Fe_3O_4 MNPs < I < V < II < IV) may be attributed to hydroxyl, carbonyl and nitrogen groups decomposition [5,29-31]. The narrow exothermic peak at 475 ^{o}C for sample I (f-succininc acid) with a weight loss of 1.3 % and at 583 ^{o}C for sample III (f-oxalic acid) with a weight loss of 2.2 % may be related to decomposition of carbonyl groups forming a stronger bond with MNPs [29-31].

The above results indicate different thermal decomposition confirming the results by FTIR-S indicating various adsorption behavior of molecules via MNPs surface interaction.
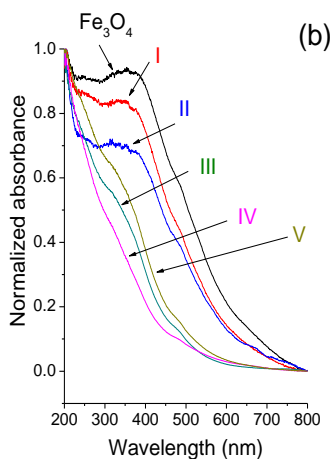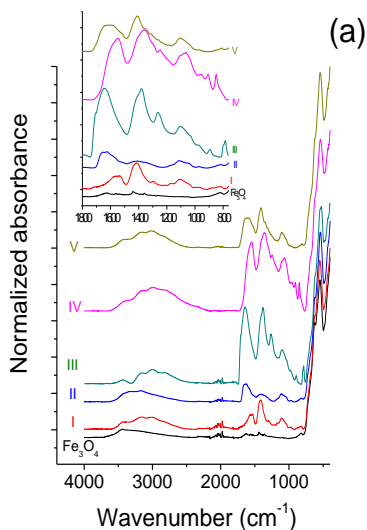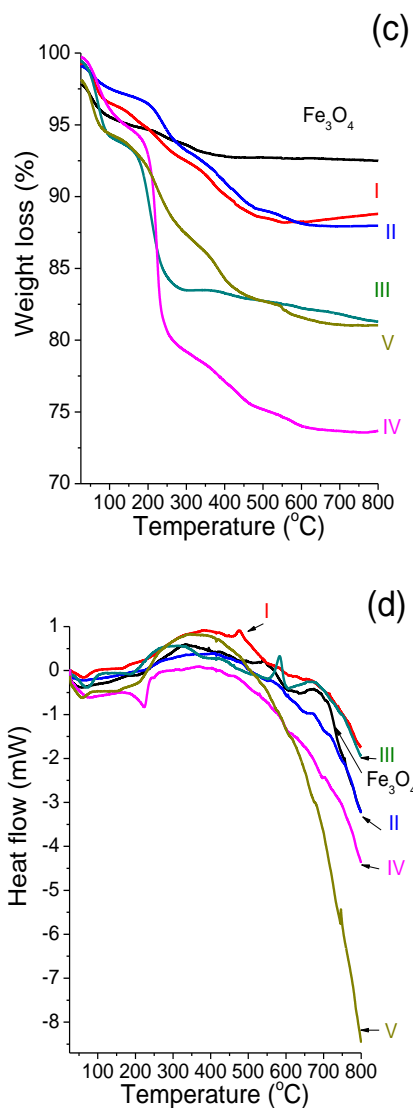
Figure 1: (A) The ATR-FTIR, (B) UV-vis spectra and (C) TGA and (D) DSC curves of the investigated Fe$_3$O$_4$ MNPs and Fe$_3$O$_4$ f-MNPs I-V.

Quantitative Surface Analysis

The survey XPS spectra (**Figure 2**) showed Fe, C, O, N and contaminations of S and Cl at the surface. The quantitative

surface analysis was performed using the peak areas (Fe 2p, C 1s, O 1s, N 1s, S 2p and Cl 2p) after Tougaard background subtraction [33] using the XPS MultiQuant software [34,35] considering a homogeneous surface distribution of elements, Scofield subshell photoionisation cross-sections [36] and correction for analyzer transmission function and electron elastic scattering. The atomic composition of samples Fe_3O_4 and I-V is listed in **Table S1.** The Fe_3O_4 MNPs show contamination of only Cl. The N from functionalizing adsorbed molecules was present in samples II and V, whereas samples III and IV indicated contamination of N. Otherwise, all f-MNPs show contamination of Cl and sample IV contamination of S. Contaminations of Cl and S result from precursors used in the Massart's synthesis of Fe_3O_4 MNPs, whereas contamination of N from ammonia and N gas flow conditions applied in the above mentioned synthesis.

Comparison of elemental ratios at the surface resulting from XPS to those in the bulk resulting from EDX, published elsewhere [3], is shown in **Figure 3**. The ratios of C/Fe and O/Fe atomic contents at the surface (XPS) are larger than the respective ratios in the bulk (EDX) indicating remarkably larger carbon and oxygen content after functionalization, which result from formation of carbon-oxygen layer at the surface of Fe_3O_4 f-MNPs. The ratio of O/C atomic content smaller at the surface than in the bulk indicates oxygen deficiency of functionalizing surface layers in comparison to the bulk Fe_3O_4 MNPs. Differences in these ratio values for MNPs and f-MNPs denoted as I-V confirm various adsorbed molecules layer of different surface coverages.
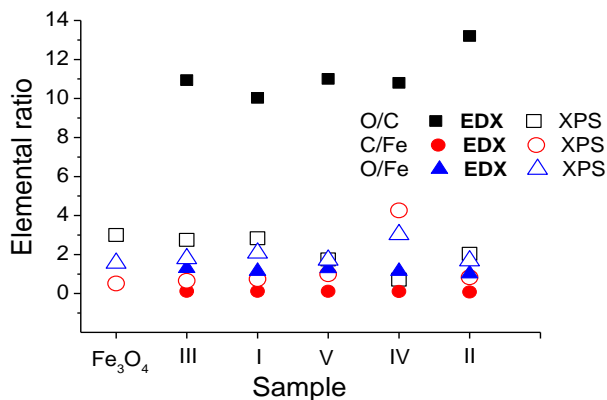
Figure 3: Comparison of ratios of elemental contents at the surface (XPS) and in the bulk (EDX) [3] of Fe_3O_4 and Fe_3O_4 f-MNPs I-V. Samples f-MNPs I-V are listed in the order of decreasing cytotoxicity.
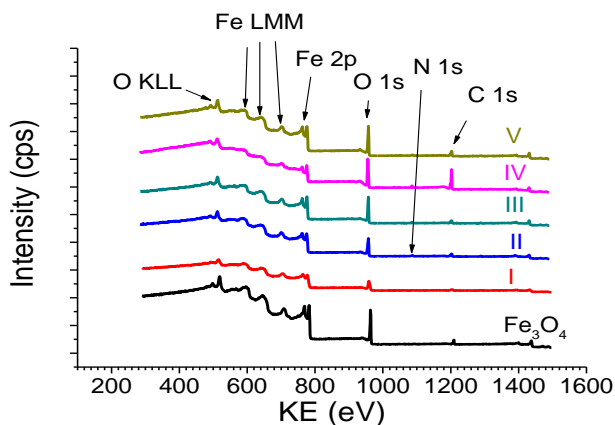
Figure 2: The survey XPS spectra recorded from Fe_3O_4 MNPs and Fe_3O_4 f-MNPs I-V.

Chemical State of Carbon, Oxygen and Nitrogen

Fitting of C 1s, O 1s and N 1s spectra was performed after Tougaard background subtraction using the XPSPeakfit41 software [37]. The fitting of C 1s, O 1s and N 1s spectra was focused on determination of the chemical forms of functionalizing overlayers and the Fe_3O_4 MNPs substrate. The expected C chemical forms at the surface of Fe_3O_4 MNPs are

carbon atoms forming sp^2 and/or sp^3 hybridizations and sp^2 and/or sp^3 carbon bonded to oxygen groups like carbonyl (C=O), hydroxyl (C-OH) and carboxyl (C-OOH) resulting from oxygen adsorption, whereas functionalization of Fe_3O_4 MNPs substrate is expected to provide increased number of carbon forms resulting from the chemical treatment with biocompatible molecules I-V, which consist mainly of C sp^2/sp^3 and carboxylic bonds (**Figure S1**). These carbon oxygen bonds resulting from oxidation of carbon layer on Fe_3O_4 MNPs and the MNPs additional functionalization, i.e. C=O, C-OH and C-OOH, are expected to be present in O 1s spectrum. However, O 1s spectrum should also provide information on oxidized forms of Fe. Previously reported experimental and theoretical results [38-42] provided and compiled the values of binding energy (BE) for C 1s and O 1s spectra typical for these carbon-oxygen groups for different carbon nanomaterials. Similarly, different oxidized forms of Fe due to iron treatment with oxygen and water were reported previously including the respective BE values [43], as well as carbon-nitrogen chemical forms [38].

The resulting C 1s, O 1s and N 1s spectra for sample III are shown in **Figure 4**, whereas the spectra recorded and fitted for all the samples are presented in **Figure S3A-C**. The atomic contents of carbon, oxygen and nitrogen chemical states resulting from C 1s, O 1s and N 1s spectra fitting are listed in **Table S2A-C**. **Table S2A-C** contains also the respective BE values for C 1s, O 1s and N 1s electrons characterizing the chemical states of the components of the adsorbed molecule layers and Fe_3O_4 substrate. At the surface of Fe_3O_4 MNPs the C-OH and C-OOH bonds are present, whereas f-MNPs I-V surfaces exhibit a large amount of C-OOH bonds (**Table S2A**) due to functionalizing adsorbed molecules consisting profoundly of carboxylic bonds (**Figure S1**). Small amount of C-OH bonds at the surface of sample III results probably from decomposition of carboxylic groups due to X-ray damage. The O 1s spectrum (**Table S2B**) indicates the same amount of C-OOH groups resulting from adsorbed molecules and iron oxide forms interpreted as the lattice O^{2-} and adsorbed O^- from Fe_3O_4 and/or FeOOH and lattice OH^- and adsorbed OH^- from FeOOH, where adsorbed forms refer to confirmed by the angular resolved

measurement forms at the outer surface [44] and finally water adsorbed at the surface. Although, O$^-$ and OH$^-$ species would adsorb as atomic or molecular form, they receive the negative charge from tunneling electrons from the metal to the surface, as it has been suggested to occur during oxidation of Fe. Therefore, the notation of adsorbed O$^-$ and OH$^-$ includes a partial negative charge, which allow their BE values to be close to BEs for the lattice O^{2-} and OH$^-$. At the surface of Fe$_3$O$_4$ MNPs and their I-V functionalized MNPs the largest amount of lattice O^{2-} is observed, then lattice OH$^-$ and then adsorbed OH$^-$ and O$^-$ forms and water. The comparison of the atomic contents of carbon and oxygen chemical states (**Table S2A-B**) for Fe$_3$O$_4$ MNPs and f-MNPs I-V in the order of decreasing cytotoxicity on HeLa cells is shown in **Figure 5A** and **B**, respectively.

Chemical State of Fe

The stoichiometric magnetite Fe$_3$O$_4$ of cubic close packed oxygen sublattice can be alternatively expressed as FeO•Fe$_2$O$_3$. Therefore, it consist of iron ions Fe^{2+} and Fe^{3+} occupying the tetrahedral (denoted as Th) and octahedral (denoted as Oh) interstices of cubic spinel type structure. The ideal Fe$_3$O$_4$ atomic ratio of Fe^{2+}: Fe^{3+} is 1:2, and precisely the ratio of Fe$_{Oh}$$^{2+}$: Fe$_{Oh}$$^{3+}$: Fe$_{Th}$$^{3+}$ is 1:1:1. The fitting of Fe 2p spectra was accounting for Fe^{2+} and Fe^{3+} octahedral and Fe^{3+} tetrahedral spectra components parameters like Fe 2p$_{3/2}$ BE and FWHM values reported in the literature [2,4,45-49] Exemplary Fe 2p spectra fitting results are shown in **Figure 4**, whereas all the fitted spectra in **Figure S4**. **Table 1** provides the parameters of the fitted Fe 2p$_{3/2}$ spectra recorded for Fe$_3$O$_4$ MNPs and f-MNPs I-V. For Fe$_3$O$_4$ MNPs the obtained values of BE for Fe^{2+} octahedral and Fe^{3+} tetrahedral and octahedral components, as well as intensity ratios of Fe^{3+} and Fe^{2+} tetrahedral and octahedral components equal to 1:1:1 are in agreement with those reported previously [45], confirming Fe$_3$O$_4$ MNPs (**Table 1**). The temperature functionalization of Fe$_3$O$_4$ surface by biocompatible admolecules (samples I-V) at 70-80 ^{o}C modifies the stoichiometry of Fe$_3$O$_4$, i.e. FeO•Fe$_2$O$_3$, leading to changes of ratio of Fe^{2+} octahedral and Fe^{3+} tetrahedral and octahedral components, their BE values, separation between the octahedral Fe^{2+} component and plasmon loss of octahedral

Fe^{2+} component (ΔFe_{Oh}^{2+}) of the Fe 2 $p_{3/2}$ spectra, which are also reflected in magnetic properties. Consistently increasing values of BE due to functionalization, values of ratio of Fe^{2+} and Fe^{3+} components and values of separation between Fe $2p_{3/2}$ octahedral 2+ component and values of separation between plasmon loss of Fe $2p_{3/2}$ octahedral 2+ component (ΔFe_{Oh}^{2+}) ranging from 8.11 eV to 8.77 eV (**Table 1**) indicate surface oxidation. Such separation values (ΔFe_{Oh}^{2+}), i.e. from 8.0 eV to 8.5. eV were observed for α- and γ- FeOOH and Fe_2O_3 [43].

As reported previously [3] the value of saturation magnetization, M_s, for Fe_3O_4 f-MNPs I-V, determined as a maximum magnetization characterized by parallel orientations of magnetic moments, varies from 45-70 emu g^{-1} as a results of nanoparticle size and surface oxidation (**Figure 6A-B**). These values are smaller than the respective value for a bulk Fe_3O_4, i.e. 89-92 emu g^{-1}, and within agreement with various size Fe_3O_4 nanoparticles modified by different organic material. Generally, the value of M_s increases with increasing nanoparticle size [48]. This remains in agreement with the results obtained by Rangam et al. [3], where increasing M_s values are observed with increasing diameters obtained from XRD (**Figure 6A**). However, diamagnetic coating of nanoparticles causes decrease of M_s due to introducing surface spin disorder. Previously reported results provided evidences on modification of magnetic properties of Fe_3O_4 due to adsorption [49], grain size [4] and functionalization [50]. The oxidation of the surface-interface of Fe_3O_4 MNPs I-V is reflected in increasing Fe $2p_{3/2}$ BE values and separation between Fe $2p_{3/2}$ octahedral 2+ component and plasmon loss of Fe $2p_{3/2}$ octahedral 2+ component (ΔFe_{Oh}^{2+}) (**Figure 6B**) justifying modification of magnetic properties resulting from slight modification of Fe_3O_4 stoichiometry and spin flipping at the interface of MNPs and functionalizing adsorbed molecules. The saturation magnetization increases in the following order: sample IV < sample II < sample III < sample V < sample I.

Table 1: The percent of Fe^{2+}/ Fe^{3+} octahedral (Oh) and Fe^{3+} tetrahedral (Th) chemical states including BE values of Fe $2p_{3/2}$ components, ratio of separation between Fe $2p_{3/2}$ octahedral 2+ component and plasmon loss, ratios of Fe_{Oh}^{2+}, Fe_{Oh}^{3+} and Fe_{Th}^{3+} components, ratio of plasmon loss to the total area and separation of Fe_{Oh}^{2+} components from plasmon loss in Fe $2p_{3/2}$ spectra recorded from Fe_3O_4 and Fe_3O_4 f-MNPs I-V. Samples f-MNPs I-V are listed in the order of decreasing cytotoxicity.

Sample	Fe chemical state						$Fe_{Oh}^{2+}/$ $Fe_{Oh}^{3+}+$ Fe_{Th}^{3+}	$Fe_{Oh}^{2+} : Fe_{Oh}^{3+} :$ Fe_{Th}^{3+}	$A_{Plas}/$ A_{Total}	ΔFe_{Oh}^{2+} - plasmon
	Fe_{Oh}^{2+}		Fe_{Oh}^{3+}		Fe_{Th}^{3+}					
	(%)	BE (eV)	(%)	BE (eV)	(%)	BE (eV)				
Fe_3O_4	33	710.0	33	711.4	34	713.3	0.49	1 : 1 :1	0.5844	8.77
III	39	710.4	38	711.9	23	713.9	0.64	1 : 0.97 : 0.59	0.5857	8.52
I	30	710.8	35	712.2	35	714.0	0.43	0.86 : 1 :1	0.5007	8.90
V	34.5	710.5	34.5	711.9	31.0	713.8	0.53	1 : 1 : 0.90	0.5855	8.32
IV	40	710.0	34	711.4	26	713.3	0.67	1 : 0.85 : 0.65	0.5986	8.11
II	37.0	710.5	39.0	712.0	24.0	714.1	0.59	0.95 : 1 : 0.62	0.5815	8.49

Chemical State of Chlorine and Sulphur Contaminations

Chlorine was observed in Fe_3O_4 and samples I-V (0.1-1.9 at. %), whereas sulphur (1.1 at. %) in sample IV (**Table S1**). The chemical states of chlorine and sulphur contaminations were analyzed by fitting of Cl 2p (**Figure 4**, **S5A**, **Table S3**) and S 2s (**Figure S5B**) spectra. Chlorine chemical states are interpreted as: (i) $[(CH_3)_4N]Cl$ and/or $[N(C_2H_5)_4]Cl$ (BE=196.6±0.3 eV), (ii) $C(NH_2)_3Cl$ (BE=198.2±0.3 eV) and (iii) Met-Cl and/or ($-CH_2CHO(Cl)-)_n$ (BE=199.9±0.3 eV) [30]. Sulphur chemical state was interpreted as $-SO_4$ (BE== 168.6 eV) [30]. The resulting BE values providing information on the chemical states of Cl and S indicate that ionic Cl and S are bonded to and Fe_3O_4 MNPs and adsorbed functionalizing molecules, what may result from segregation due to applied temperature conditions (70 ^{o}C-80 ^{o}C) during functionalization of MNPs.
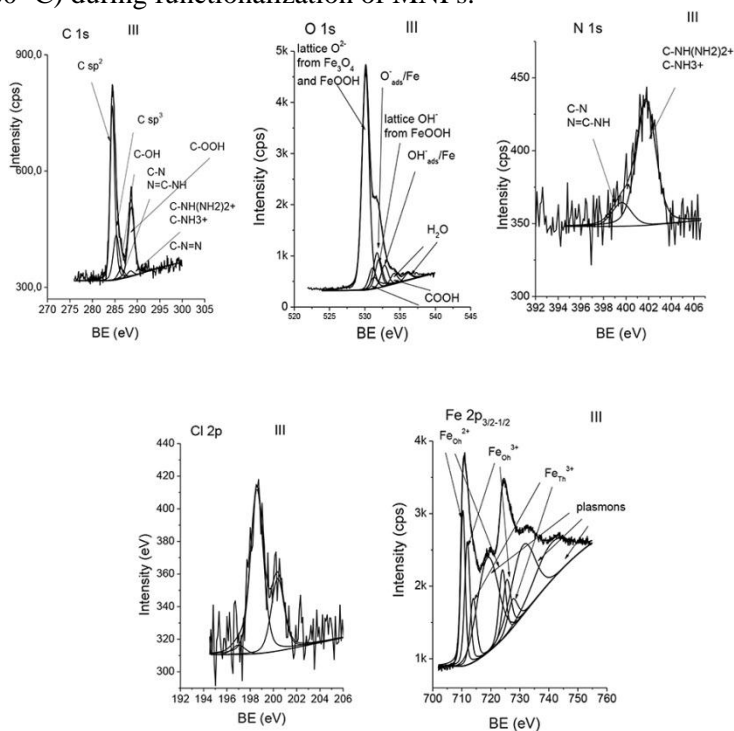

Figure 4: The XPS C 1s, O 1s, N 1s, Cl 2p and Fe 2p spectra fitted to different chemical forms for exemplary Fe_3O_4 f-MNPs III.
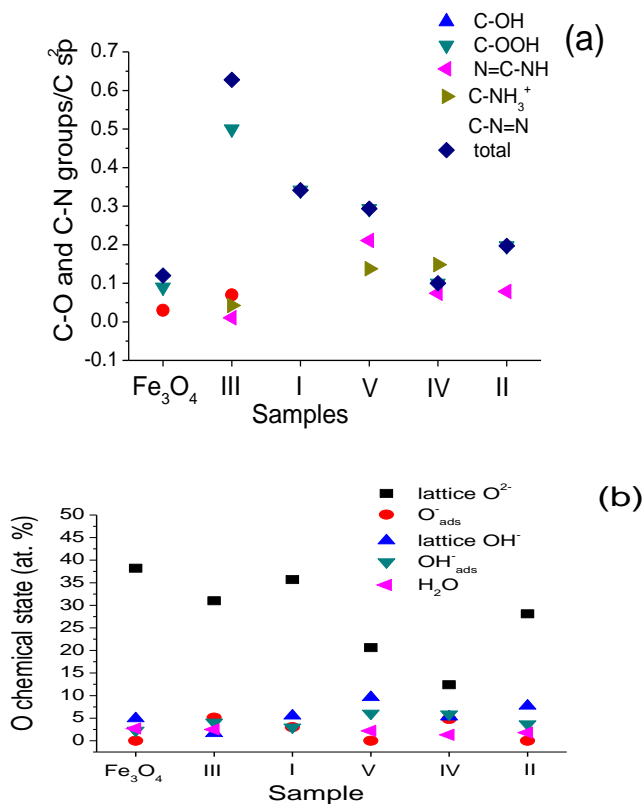
Figure 5: Contents of (A) carbon-oxygen and carbon-nitrogen groups resulting from fitting of C 1s spectra normalized to C sp^2 and (B) oxygen chemical states resulting from fitting of O 1s spectra in Fe$_3$O$_4$ MNPs and Fe$_3$O$_4$ f-MNPs I-V. Samples f-MNPs I-V are listed in the order of decreasing cytotoxicity.
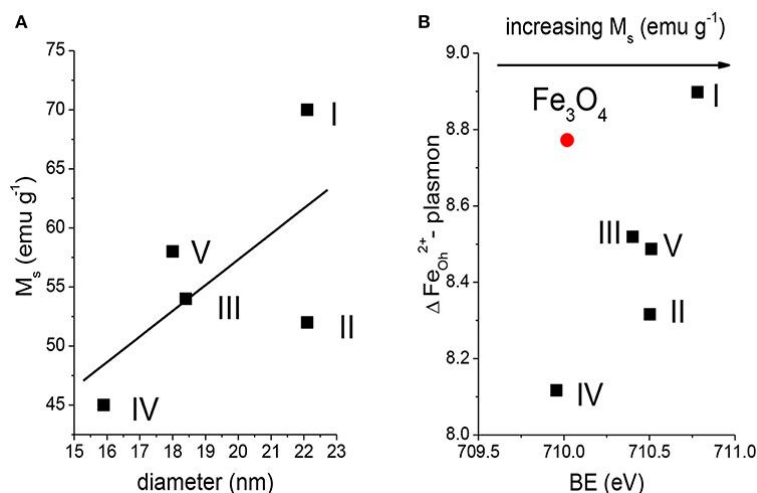
Figure 6: Dependence of (A) Fe_3O_4 f-MNPs I-V diameters determined from XRD [3] as a function of saturation magnetization. (B) BE of Fe 2p 2+ octahedral component on separation between Fe $2p_{3/2}$ 2+ octahedral component and plasmon loss in Fe $2p_{3/2}$ spectra recorded from Fe_3O_4 MNPs and Fe_3O_4 f-MNPs I-V.

Auger Parameters

The Auger parameters are not sensitive to uniform charging of nonconductive specimens. Combining information resulting from photoelectron peak positions and peak positions of the Auger transitions (**Figure 7**), providing the Auger parameters, is a powerful tool for exploring the electronic structure of surfaces and interfaces in XPS-XAES studies.
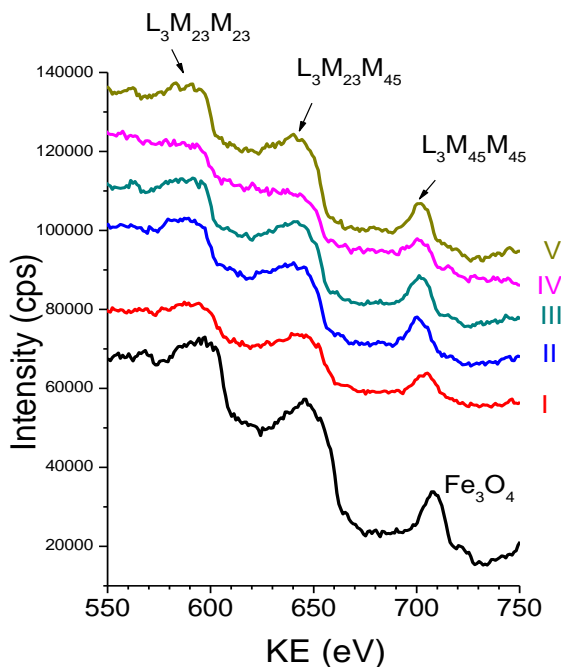
Figure 7: The Fe L$_3$VV Auger spectra recorded from Fe$_3$O$_4$ MNPs and Fe$_3$O$_4$ f-MNPs I-V.

The local electronic changes in charge redistribution and transfer at atomic level can be investigated analyzing the final state Auger parameter (Eq. (1a)) and the initial state Auger parameter (Eq. (1b) defined as [30,51]:

$$\alpha = E_A + E_B \qquad\qquad\qquad\qquad\text{Eq. (1a)}$$

$$\beta = E_A + 3E_B, \qquad\qquad\qquad\qquad\text{Eq. (1b)}$$

where E$_A$ is the kinetic energy (KE) of the Auger electron and E$_B$ is the binding energy (BE) of the photoelectron. Changes in the Auger parameter between two environments due to the atomic potentials in the core of the atom and the core hole screening efficiency (extra-atomic relaxation), ΔR, (Eq. (2a), as well as between atomic potentials in the core of the atom at the atomic site, ΔV, (Eq. (2b)) are defined as [52,53]:

$$\Delta\alpha = \alpha_{Fe3O4t} - \alpha_{env} = 2\Delta R \qquad\qquad\qquad \text{Eq. (2a)}$$

$$\Delta\beta = \beta_{Fe3O4} - \beta_{env} = 2\Delta V, \qquad\qquad\qquad \text{Eq. (2b)}$$

where α_{env} and β_{env} refer to functionalized Fe_3O_4 MNPs surface. The final state effects (ΔR) refer to a shift in polarization energy at the core-ionised atom. This shift considers the charge transfer in a local valence band orbital of the core ionised atom and the contribution to the electronic relaxation energy of all the other atoms in the system. The initial state effects (ΔV) represent a chemical shift as a result of a ground state electronic structure and depend on bonding to neighbouring atomic valence states. This shift is related to electronic states like e.g. band structures, bond directionality and structural parameters like atomic positions and Madelung constants of the bonded atom.

The Wagner plot for a given element and/or compound, known also as chemical state plot or chemical state diagram, displays in a compact form the values of photoelectron BE, Auger electron KE and Auger parameters. Positions of compounds on this plot indicate relaxation shifts of various species, initial and final state effect contributions of various species. Therefore, Wagner plot information is related to concept of ionicity, electronegativity and polarizability. The Wagner plots for Auger Fe $L_3M_{45}M_{45}$ electrons – Fe $2p_{3/2}$ photoelectron spectra and Auger O KLL electrons – O 1s photoelectron spectra representing the investigated Fe_3O_4 and Fe_3O_4 MNPs I-V samples are shown in **Figure 8**, whereas values of Auger spectra KE, BE of photoelectron spectra and Auger parameters resulting from Eq. (1a-b) – (2a-b) are provided in **Table S4A-B**. It should be noted that Eq. (2a-b) are good approximation in the case of core-core-core Auger transitions.
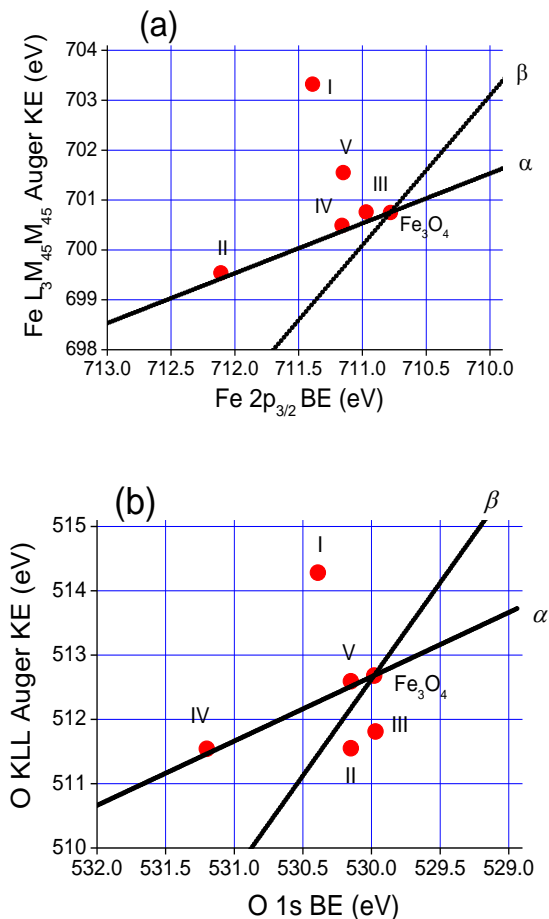
Figure 8: Wagner plots for (A) Fe $L_3M_{45}M_{45}$ and Fe $2p_{3/2}$ spectra and (B) O KLL and O 1s spectra representing the investigated Fe_3O_4 MNPs and Fe_3O_4 f-MNPs I-V.

The spectral shape of Auger transition (**Figure 7**) is influenced by the valence band density of states and also by changes in the local density of states resulting from the screening of the initial core-hole. Therefore, any change of Auger spectral profile indicates modification of the local density of states. The core-core-core Auger electrons ($L_3M_{23}M_{2.3}$) are not involved into bonding in contrary to core-core-valence Auger electrons ($L_3M_{23}M_{45}$). The number of electrons from Fe atom in the d

states of the valence band, n^d, evaluated from the ratio of core-core-valence to core-core-core Auger intensities [54] decreases in the following order: 0.92 (sample I), 0.89 (Fe_3O_4 MNPs), 0.86 (sample III), 0.85 (samples II and IV) and 0.83 (sample V) and exhibits no direct relation with cytotoxicity.

Overlayer Thickness

The thickness of adsorbed molecules overlayers was evaluated using the following methods:

1. QUASES-Analyze [55],
2. XPS MuliQuant [34,35] and
3. attenuation equation [56]

and applying the inelastic mean free path (IMFP) values of photoelectrons from the G1 equation of Gries [57].

QUASES-Analyze [55], evaluates the surface morphology, i.e. type of depth profile, percent coverage and layer thickness from XPS spectra and an inelastic background in the vicinity of the photoelectron peak. Exemplary results of QUASES-Analyze evaluations using the Buried Layer (BL) model without a standard and models of BL and Active Substrate (AS) with a Fe_3O_4 standard are shown in **Figure S6A-C**, respectively. The values of surface coverage, adsorbed molecules overlayer thickness resulting from QUASES-Analyze BL and AS models without and with Fe_3O_4 standard and averaged overlayer thickness are listed in **Table 2**.

Table 2: Coverage and overlayer thickness resulting from QUASES-Analyze Buried Layer (BL) model without a standard, BL and Active Substrate (AS) models with Fe$_3$O$_4$ standard. Evaluation is performed from Fe 2p$_{3/2}$ spectra recorded from Fe$_3$O$_4$ and Fe$_3$O$_4$ f-MNPs I-V. Samples f-MNPs I-V are listed in the order of decreasing cytotoxicity.

Sample	Analyze BL No standard Thickness (nm)	Analyze BL Cov. (%)	Analyze BL Thickness (nm)	Analyze AS Thickness (nm)	Av. Thickness (nm)
III	1.34	50.6	1.19	1.2	1.24±0.08
I	1.5	42.2	1.6	1.58	1.56±0.05
V	1.51	70.5	1.58	1.59	1.56±0.04
IV	2.38	61.0	2.26	2.27	2.30±0.07
II	1.38	58.9	1.5	1.5	1.46±0.07

Table 3: Parameters for determining overlayer thickness from XPS MultiQuant [34,35], attenuation equation (Eq. (3)) [56], IMFP values for various overlayers from Gries G1 equation [57] and comparison of overlayer thickness values resulting from XPS MultiQuant, attenuation equation and effective thickness from QUASES-Analyze for Fe$_3$O$_4$ MNPs and Fe$_3$O$_4$ f-MNPs I-V. Samples f-MNPs I-V are listed in the order of decreasing cytotoxicity. The IMFP values were calculated for Fe 2p$_{3/2}$ photoelectrons kinetic energy.

Sample	Density (g cm^{-3})	Atomic weight (g mol^{-1})	N$_v$	overlayers IMFP$_{Gries}$ (nm)	t (nm) Eq. (3) (IMFP$_{Gries}$)	t (nm) XPS MultiQuant (IMFP$_{Gries}$)	Effective Av. Thickness QUASES-Analyze (nm) (IMFP$_{Gries}$)
Fe$_3$O$_4$	5.18	231.533		1.55			
III	1.90	90.03 (anhydrous)	34	2.20	1.0	1.11	0.63
I	1.56	118.09	46	2.06	0.74	0.68	0.66
V	1.4601	147.13	58	2.11	1.42	1.04	1.10
IV	1.665	192.12 (anhydrous)	74	2.16	1.22	-	1.40
II	1.43	174.20	70	2.00	1.37	0.66	0.86

Table 4: Dependence of cytotoxicity tested for HeLa cells on surface properties of Fe3O4 f-MNPs I-V. Samples f-MNPs I-V are listed in the order of decreasing cytotoxicity. Symbols denote: DH – hydrodynamic diameter, PDI – polydispersity.

Sample	Av.% cell death	Cov. (%)	Av. t (nm)	C-OOH +C-OH C 1s (at. %)	Total O/C sp^2 C 1s	Lattice O^{2-}+OH$^-$ /C sp^2	Ads (O$^-$+OH$^-$)$_{ads}$ /C sp^2	D$_H$ (nm)	PDI	Zeta Potential (mV)	Overlayer Interaction with MNPs
Fe$_3$O$_4$	-	-	-	1.7	0.12	3.01	0.16	601.3	0.171	0.56	-
III	10.8	50.6	0.91	5.4	0.57	3.47	0.98	217.9	0.853	0.83	weaker
I	10.7	42.2	0.69	4.3	0.34	3.27	0.48	527.9	0.101	-0.53	stronger
V	9.2	70.5	1.19	3.2	0.29	2.77	0.56	256.7	0.246	0.28	stronger
IV	7.5	61.0	1.31	3.1	0.10	0.57	0.35	717.7	0.039	0.19	stronger
II	5.3	58.9	0.96	2.5	0.20	0.36	0.29	871.2	0.237	-0.23	stronger

The thickness resulting from XPS MultiQuant [34,35] was evaluated using the Layers-on-Sphere model. Although the particles are small, the large difference between the IMFP of the overlayer and a core allows using it (particle radius set to 10 nm). The composition, molecular weight and IMFP values from G1 equation [57] for each adsorbed molecules are listed in **Table 3**. Other parameters applied are: Al K$_\alpha$ excitation, Scofield cross-section, Reilman angular corrections for analyzer input angle of 54.4°. The surface of Fe$_3$O$_4$ nanoparticles is oxygen deficient in comparison to functionalized nanoparticles I-V (**Figure 3**). After functionalization the calculated thickness of contamination assuming CH$_x$ hydrocarbon and possible other oxidized states (Table 1) is almost the same but quantity of the missing oxygen is different. Due to the oxygen deficiency of the nanoparticles and their original carbonaceous contamination, the calculated layer thickness must be considered critically; presumably, the values calculated without oxygen are closer to reality. In the case of nitrogen containing molecules, the nitrogen deficiency suggests that beside the adsorbed molecules, carbonaceous contamination is also present. It may be true for the other molecules as well. The values of overlayer thickness evaluated from XPS MultiQuant are listed in **Table 3**.

The following attenuation equation was applied [56]:

$$t = \lambda \cos \alpha \ln(R+1), \qquad\qquad \text{Eq. (3)}$$

where λ is the IMFP from Gries G1 equation [57] and R is given by Eq. (4):

$$R = \left(\frac{I_i^l}{I_j^s} \right) \left(\frac{I_j^o}{I_i^\infty} \right), \qquad\qquad \text{Eq. (4)}$$

where I_i^∞ is the intensity of the photoelectron signal from an infinitely thick layer, I_j^o is the signal intensity from the uncovered substrate, I_i^l is the intensity of photoelectron signal from a layer of a thickness t and I_j^s is the intensity of

photoelectron signal from a substrate covered by a layer of thickness *t*.

The $\dfrac{I_i^{\infty}}{I_j^{o}}$ can be measured in a separate experiment and/or calculated from Eq. (5):

$$\frac{I_i^{\infty}}{I_j^{o}} = \frac{S(E_i)M^{l}\lambda_i^{l}(d\sigma_x / d\Omega)_i}{S(E_j)M^{s}\lambda_j^{s}(d\sigma_x / d\Omega)_i},$$
Eq. (5)

where *S* is the spectrometer function, $d\sigma_x / d\Omega$ is a differential photoelectric cross-section, *M is* atomic density of a given element (number of atoms in unit volume), $M = \dfrac{N_o \rho}{A}$, N_o is Avogadro number, λ_i^{l} is the IMFP for photoelectrons emitted in a layer *l* and moving in a layer *l*, λ_j^{s} is the IMFP for photoelectrons emitted in a substrate *s* and moving in a layer *l*, ρ is a density, *A* is atomic mass and α is a detection angle with respect to the surface normal. The values of parameters for determining the layer thickness from Eq. (3), IMFPs from Gries G1 equation [57], the layer thickness resulting from Eq. (3) are provided in **Table 3**. Comparison of adsorbed molecules layer thicknesses obtained from QUASES-Analyze (so-called effective layer thickness, i.e. layer thickness multiplied by a coverage), XPS MultiQuant and attenuation equation (Eq. (3)), respectively, is provided in **Table 3** and **Figure 9**.
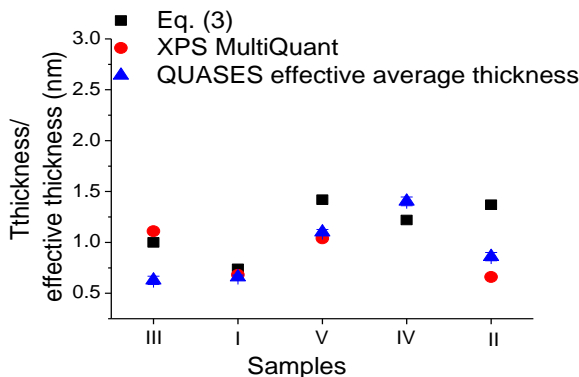
Figure 9: Comparison of overlayer thickness resulting from attenuation equation (Eq. (3)) (solid square), XPS MultiQuant (solid circle) and effective average thickness resulting from QUASES-Analyze (solid triangle) for Fe_3O_4 f-MNPs I-V. Samples f-MNPs I-V are shown in the order of decreasing cytotoxicity.

REELS Spectra

Comparison of REELS spectra recorded from Fe_3O_4 MNPs and f-MNPs I-V and parameters derived from these spectra are shown in **Figure 10**. The electron scattering probabilities (elastic peak intensities) at 0 eV and inelastic scattering probabilities on valence band electrons in the region of about 80 eV above the elastic peak (electron inelastic losses) show variations due to functionalization (**Figure 10A-B**) with no remarkable changes in elastic peak full width at half maximum (FWHM) of 0.83±0.02 eV. The presented changes (**Figure 10A-B**) reflect modification of surface electronic and optical properties. The quantitative analysis of REELS spectra combined with Tougaard QUEELS algorithm [58] may provide detailed information on parameters of surface electronic and optical properties [58-60]. The band gap energy (E_g) value can be evaluated from REELS spectra since the plasmon loss peak exhibiting broad peaks with the energy in the vicinity of the elastic peak at 0 eV appears below the electron-hole interband transition. The onset of the loss spectrum is due to electron-hole excitation. The band gap energy was estimated from a linear fit line along the maximum negative slope at a point near the onset of the loss signal spectrum to the

background level. The crossing of the linear fit line and the background level provides the band gap value (**Figure 10C**). The band gap energy values for Fe_3O_4 MNPs is 2.45 eV similarly as reported previously, i.e. 2.5 eV [60]. These values for Fe_3O_4 f-MNPs increase from 2.45 eV to 2.7 eV and exhibit decreasing dependence of band gap energy with decreasing carbon content and increasing nanoparticle size (**Figure 10D**). Similarly, increasing band gap energy values, i.e. from 2.4 eV to 2.9 eV, with increasing carbon content in Fe_3O_4 [59] and decreasing Fe_3O_4 nanoparticle size [61] were reported previously. The inelastic scattering probability values showing changes due to functionalization (**Figure 10A-D**) provide evidences on modified optical and dielectric properties of the investigated surface [59]. No direct dependence of band gap energy of f-Fe_3O_4 MNPs on cytotoxicity tested for HeLa was observed, although this cytotoxicity was the highest for sample III of an intermediate nanoparticle size, the lowest carbon content and the band gap energy value closest to the that for Fe_3O_4.

Dependence of Cytotoxicity Tested for HeLa Cells on Surface Properties of Functionalized Fe_3O_4 Nanoparticles

Compilation of features indicating the differences in structural and chemical properties in the investigated surfaces Fe_3O_4 f-MNPs I-V in the order of decreasing cytotoxicity is compiled in Table 4. The highest cytotoxicity is observed for Fe_3O_4 f-MNPs with (i) the smaller surface coverage and thickness of biocompatible adsorbed molecules layers, (ii) the highest content of oxygen and carbon-oxygen functionalizing groups, (iii) the highest ratio of lattice O^{2-} and OH^- to C sp^2 hybridizations on MNPs surface, (iv) the highest ratio of adsorbed O^- and OH^- to C sp^2 hybridizations due to adsorbed molecule layers, (v) the closest electronic and optical properties to Fe_3O_4 shown in Auger parameters of XPS and Auger lines from Fe (Figure 8A) and REELS spectra (Figure 10A-D). No dependence of Cl and S contaminations and band gap energy was observed. No dependence of cytotoxicity on PDI and Zeta potential values in the recorded range was shown. This would indicate that for the applied conditions of concentration, temperature and pH the

samples homogeneity and ability for attachment to a negatively charged cell membrane is less important than content of adsorbed molecules oxygen groups, which are responsible for generating ROS. Higher cytotoxicity is observed for MNPs of smaller hydrodynamic diameters (217.9-527.9 nm) indicating that adlayers of smaller polymerization degree will favor ROS generation.

Although, different iron oxides and also Fe_3O_4 have been previously applied for diagnosis and in tumor therapy [1], the biocompatibility of functionalized Fe_3O_4 MNPs is competitive to Fe_3O_4 nanoparticles. The enhanced cytotoxicity for HeLa cells has been previously reported for L-cysteine-conjugated ruthenium oxy-hydroxide ($RuO_x(OH)_y$) in comparison to $RuO_x(OH)_y$ [62]. This cytotoxicity of L-cysteine-conjugated ($RuO_x(OH)_y$) increasing with the concentration of this agent was attributed to selective ability of HeLa cells to create bonding with this surface. According to the above, the cytotoxicity of f-MNPs seems to be related with interaction of cells with the applied agent surface, where both oxygen groups, Fe_3O_4 lattice O^{2-} and OH^- and adsorbed O^- and OH^- play a role of adsorption and catalytic sites leading to the cytotoxicity of HeLa cells. Cytotoxicity was found to be higher for systems with a larger amount of double-carboxylic groups, which could enhance kinetics of Fenton reaction.
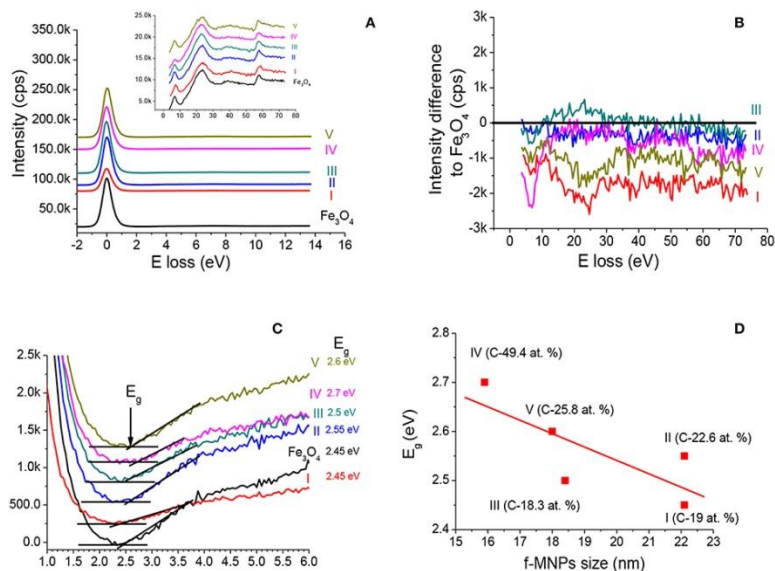
Figure 10: (A) Comparison of elastic peak and spectrum of inelastic losses of electrons on valence band electrons recorded from Fe_3O_4 MNPs and f-MNPs. (B) Differences between the spectrum of inelastic losses of electrons on valence band electrons recorded from Fe_3O_4 f-MNPs and the respective spectrum recorded from Fe_3O_4 MNPs. (C) Evaluation of band gap energy values from REELS spectra recorded from Fe_3O_4 MNPs and f-MNPs. (D) Dependence of band gap energy values on Fe_3O_4 f-MNPs nanoparticle size [3] and surface carbon content (**Table S1**).

Conclusions

Functionalization of Fe_3O_4 MNPs with different adsorbed molecules (samples I-V) to increase biocompatibility of Fe_3O_4 MNPs provides no modification in biocompatibility on L929 cells. However, it leads to variation in cytotoxicity on HeLa cells decreasing in the order III ≈ I > V > IV > II due to chemical and morphology modification of Fe_3O_4 MNPs.

The adsorbed layers provide f-MNPs of various physico-chemical properties since adsorption of amino acids leads to modification of their surface and interface providing nanoparticles of different hydrodynamic diameter, polydispersity and Zeta potential. Functionalization provides adsorbed layers on Fe_3O_4 MNPs of various thickness and partial dissolution of

oxalic, glutamic and citric acids in nanoparticles. The presence of Fe_3O_4 MNPs and adsorbed layer of different thickness is confirmed by FTIR-S and UV-vis absorption spectra. The adlayer thickness values resulting from UV-vis and QUASES are in a reasonable agreement. The adsorbed layers have different degree of polymerization confirmed by hydrodynamic diameter value. Adsorption behavior of amino acids on MNPs confirmed by FTIR-S results in s weaker (oxalic acid) and/or stronger (succinic, L-arginine, citric, glutamic acids) interactions between adlayers and MNPs and different Zeta potential values of nanoparticles. The C/O atomic contents ratio is larger at the surface than in the bulk indicating formation of functionalizing carbon-oxygen layers with oxygen deficiency in comparison to Fe_3O_4 MNPs. These carbon-oxygen layers show C sp^2, C sp^3, carboxyl (C-OOH) groups and also C-N, C-NH_3^+, C-NO_2, C-NO_3 from adsorbed molecules layers present at the surface, whereas Fe_3O_4 MNPs and f-MNPs show the presence of lattice O^{2-} and OH^- and adsorbed O^- and OH^-. The coverage of functionalizing adsorbed layers is 40-50% (oxalic and succinic acids) and 60-70% (L-arginine, citric and glutamic acid) and overlayer effective thickness is 0.69-1.31 nm. Such functionalization influences the magnetic, electronic and optical properties of Fe_3O_4 MNPs. The modification of magnetic properties is manifested in changes of ratio of Fe $2p_{3/2}$ 2+ and 3+ tetrahedral and octahedral components and separation of Fe $2p_{3/2}$ photoelectron transition from inelastic plasmon. Modification of surface electronic charge redistribution, electronic and optical properties of f-MNPs is shown in the Auger parameters (derived from XPS and Auger spectra) and elastic/inelastic scattering probabilities of electrons on atoms and valence band electrons (derived from REELS spectra).

No dependence of cytotoxicity on polydispersity and Zeta potential of Fe_3O_4 f-MNPs is observed, whereas the highest cytotoxicity is observed for f-MNPs of (i) lower degree of polymerization, (ii) the smaller surface coverage and thickness of biocompatible adsorbed molecules layers, (iii) the highest content of oxygen and carbon-oxygen functionalizing groups, (iv) the highest ratio of lattice O^{2-} and OH^- to C sp^2 hybridizations on MNPs surface, (v) the highest ratio of adsorbed O^- and OH^- to C sp^2 hybridizations on adsorbed

molecule layers, (vi) the closest electronic and optical properties to Fe_3O_4 shown in Auger parameters of XPS and Auger lines from Fe and REELS spectra. No dependence of Cl and S contaminations, band gap energy and number of electrons from Fe atom in the d states of the valence band was observed.

The enhancement of cytotoxicity of f-MNPs is related with interaction of cells with these surfaces, where both oxygen groups and increasing content of lattice O^{2-} and OH^-, as well as adsorbed O^- and OH^- from biocompatible layers play a role of adsorption and catalytic sites and a large amount of double-carboxylic groups enhancing kinetics of Fenton reaction leading to cell damage. Since the cell viability, type and mechanism of cell death is a more complex process the results of the present work provide an indicative comparison of toxicity of the nanoparticles observed for HeLa cells focusing on nanoparticles surface properties and possible HeLa adsorption behavior.

References

1. Sangaiya P, Jayaprakash R. A review on iron oxide nanoparticles and their biomedical applications. J. Supercond. Novel Magnetism. 2018; 31: 3397-3413.
2. Liu Y, Cui T, Li Y, Zhao Y, Ye Y, et al. Effects of crystal size and sphere diameter on static magnetic and electromagnetic properties of monodisperse Fe3O4 microspheres. Mat. Chem. Phys. 2016; 173: 152-160.
3. Rangam N, Sahu NK, Jaiswal A, Jayesh B. Synthesis of surface grafted mesoporous magnetic nanoparticles for cancer therapy. J. Nanosci. Nanotech. 2017; 17: 5181-5188.
4. Petran A, Radu T, Borodi G, Nan A, Suciu M, et al. Effects of rare earth doping on multi-core iron oxide nanoparticles properties. Appl. Surf. Sci. 2018; 428: 492-499.
5. Linh PH, Chien NV, Dung DD, Nam PH, Hoa DT, et al. Biocompatible nanoclusters of O-carboxymethyl chitosan-coated Fe_3O_4 nanoparticles: synthesis, characterization and magnetic heating efficiency. J. Mater. Sci. 2018; 53; 8887-8900.
6. Mahdavi M, Namvar F, Ahmad MB, Mahamad R. Green biosynthesis and characterization of magnetic iron oxide (Fe_3O_4) nanoparticles using seaweed (Sargassum muticum). Molecules. 2013; 18; 5954-5964.

7. Hu Y, Liu W, Wu F. Novel multi-responsive polymer magnetic microgels with folate or methyltetrahydrofolate. RSC Adv. 2017; 7; 10333-10344.
8. Taghavi F, Saljooghi AS, Gholizadeh M, Ramezani M. Deferasirox-coated iron oxide nanoparticles as a potential cytotoxic agent. Med. Chem. Commun. 2016; 7; 2290-2298.
9. Sahu NK, Gupta J, Bahadur D. PEGylated FePt-Fe$_3$O$_4$ composite nanoassemblies (CNAs): in vitro hyperthermia, drug delivery and generation of reactive oxygen species (ROS). Dalton Trans. 2015; 44: 9103-9113.
10. Tomitaka A, Yamaga T, Takemura Y. Magnetic nanoparticle hyperthermia using pluronic-coated Fe3O4 nanopartilces: An in vitro study. J. Nanomaterials. 2015; 5.
11. Kim DH, Kim KN, Kim KM, Lee YK. Tageting to carcinoma cells with chitosan- and starch-coated magnetic nanoparticles for magnetic hyperthermia. J. Biomaterials Research Part A. 2009; 88: 1-11.
12. Kim J. Jung J, Lee J, Na K, Park S, et al. Amphiphilic comblike polymers enhance the colloidal stability of Fe$_3$O$_4$ nanoparticles. Colloids and Surfaces B: Biointerfaces. 2010; 76: 236-240.
13. Gupta AK, Gupta M. Cytotoxicity suppression and cellular uptake enhancement of surface modified magnetic nanoparticles. Biomaterials. 2005; 26: 1565-1573.
14. Massart R. Preparation of aqueous magnetic liquids in alkaline and acidic media. IEEE Transactions on Magnetics. 1981; 17: 1247-1248.
15. Runowski M, Lis S. Synthesis, surface modification/decoration of luminescent-magnetic core/shell nanomaterials, based on the lanthanide doped fluorides (Fe$_3$O$_4$/SiO$_2$/NH$_2$/PAA/LnF$_3$). J. Luminescence. 2016; 170: 484-490.
16. Kövér L, Varga D, Cserny I, Tóth J, Tőkési J. Some applications of high-energy, high-resolution Auger-electron spectroscopy using Bremsstrahlung radiation. Surf. Interface Anal. 1992; 19: 9-15.
17. Bordbar AK, Rastegari AA, Amiri R, Ranjbakhsh E, Abbasi M, et al. Characterization of modified magnetite nanoparticles for albumin immobilization. Biotechnology Research International. 2014; 6 pages; ID 705068.

18. Asgari S, Fakhari Z, Berijani S. Synthesis and characterization of Fe_3O_4 magnetic nanoparticles coated with carboxymethyl chitosan grafted sodium methacrylate. Nanostructures. 2014; 4; 55-63.

19. Wei Y, Han B, Hu X, Lin Y, Wang X,et al. Synthesis of Fe_3O_4 nanoparticles and their magnetic properties. Procedia Engineering. 2012; 27; 632-637.

20. Kumar S, Rai SB. Spectroscopic studies of L-arginine molecule. Indian J. Pure Appl. Physics. 2010; 48; 251-255.

21. Sengupta PK, Krimm S. Vibrational analysis of peptides, polypeptides, and proteins. Biopolymers. 1985; 24: 1479-1491.

22. Silverstein RM, Bassler GC, Morrill TC. Spectrometric identification of organic compounds. 4th ed. New York: John Wiley and Sons. 1981. Available Online at: http://www2.ups.edu/faculty/hanson/Spectroscopy/IR/IRfreq uencies.html

23. Krishnan S, Raj JC, Robert R, Ramanand A, Das JS. Growth and characterization of succinic acid single crystals. Cryst. Res. Technol. 2007; 42: 1087-1090.

24. Muthuselvi C, Arunkumar A, Rajaperumal G. Growth and characterization of oxalic acid doped with tryptophan crystal for antimicrobial activity. Der Chimica Sinica. 2016; 7: 55-62.

25. Bichara LC, Lanús HE, Ferrer EG, Gramajo MB, Brandán SA. Vibrational study and force field pf the citric acid dimer based on the SQM methodology. Advances of Physical Chemistry. 2011; 10 pages; ID 347072.

26. Infrared Spectroscopy-MSU Chemistry. Available Online at: http://www2.chemistry.msu.edu/faculty/reusch/virttxtiml/Sp ectrpy/InfraRed/infrared.htm

27. Bahadur A, Saeed A, Shoaib M, Iqbal S, Bashir MI, et al. Eco-friendly synthesis of magnetite (Fe_3O_4) nanoparticles with tunable size: Dielectric, magnetic, thermal and optical studies. Materials Chemistry and Physics. 2017; 198; 229-235.

28. Bian J, Wang Y, Zhang Q, Fang X, Feng J, et al. Fatty acid decarboxylation reaction kinetics and pathway of co-conversion with amino acids on supported iron oxide catalysts. RSC Adv. 2017; 7: 47279-47287.

29. Lesiak B, Zemek J, Jiricek P, Stobinski L. Temperature modification of oxidized multiwall carbon nanotubes studied by electron spectroscopy methods. Phys. Status Solidi B. 2009; 246: 2645-2649.

30. Stobinski L, Lesiak B, Zemek J, Jiricek P, Biniak S, et al. Studies of Oxidized Multiwall Carbon Nanotubes in the Temperature Range from RT to 630 ^{o}C by the infrared and Electron Spectroscopy Methods. J. Alloys Comp. 2010; 505: 379-384.

31. Stobinski L, Lesiak B, Zemek J, Jiricek P. Time dependent thermal treatment of oxidized MWCNTs studied by the electron and mass spectroscopy methods. Appl. Surf. Sci. 2012; 258: 7912-7917.

32. Panias D, Taxiarchou M, Paspaliaris I, Kontopoulos A. Mechanisms of dissolution of iron oxides in aqueous oxalic acid solutions. Hydrometallurgy. 1996; 42; 257-265.

33. Tougaard S. Background analysis of XPS/AES-QUASES Simple backgrounds, ver. 2.2, Tougaard Inc. 1999-2001. Available Online at: http://www.quases.com

34. Mohai M. XPS MultiQuant: multimodel XPS quantification software. Surf. Interface Anal. 2004; 36: 828-832.

35. Mohai M. Multimodel of X-ray photoelectron spectroscopy quantification program for 32-bit Windows, XPS MultiQuant, ver. 7. 1999-2001.

36. Scofield H. Hartree-Slater Subshell Photoionization Cross-sections at 1254 and 1487 eV. J. Electron Spectrosc. Relat. Phenom. 1976; 8: 129-137.

37. Kwok RWM. XPS peak fitting program for WIN95/98 XPSPEAK, ver. 4.1, Department of Chemistry. The Chinese University of Hong Kong. 2000. Available Online at: rmkwok@cuhd.edu.hk.

38. Wagner CD, Naumkin AV, Kraut-Vass A, Allison JW, Powell CJ, et al. NST X-ray Photoelectron Database, NIST SRD 20, ver. 4.1, online, PC. 2012.

39. Butenko YV, Krishnamurthy S, Chakraborty AK, Kuznetsov VL, et al. Photoemission study of onion like carbons produced by annealing nanodiamonds. Phys. Rev. B 2015; 71: 075420-10.

40. Lesiak B, Kövér L, Tóth J, Zemek L, Jiricek P, et al. C sp^2/sp^3 hybridisations in carbon nanomaterials – XPS and (X)AES study. Appl. Surf. Sci. 2018; 452: 223-231.

41. Fujimoto A, Yamada Y, Koinuma M, Sata S. Origins of sp^{3}C peaks in C_{1s} X-ray photoelectron spectra of carbon materials. Anal. Chem. 2016; 88: 6110-6114.

42. Shim SH, Kim KT, Lee YU, Jo WH. Facile method to functionalize graphene oxide and its application to poly(ethylene terephthalate)/graphene composite. ACS Appl. Mater. Interfaces. 2012; 4: 4184-4191.

43. Grosvenor AP, Cobe BA, McIntyre NS. Examination of the oxidation of iron by oxygen using X-ray photoelectron spectroscopy and QUASES. Surf. Sci. 2004; 565: 151-162.

44. Grosvenor AP, Cobe BA, McIntyre NS. Studies of the oxidation of iron by water vapour using X-ray photoelectron spectroscopy and QUASES. Surf. Sci. 2004; 572: 217-227.

45. Poulin S, França R, Moreau-Bélanger L, Sacher E. Confirmation of X-ray photoelectron spectroscopy peak attributions of nanoparticulate iron oxides, using symmetric peak component line shapes. J. Phys. Chem. C. 2010; 114: 10711-10718.

46. Eltouny N, Ariya PA. Competing reactions of selected atmospheric gases on Fe_3O_4 nanoparticles surfaces. Phys. Chem. Chem. Phys. 2014; 6: 23056-23066.

47. Yamashita T, Hayes P. Analysis of XPS spectra of Fe^{2+} and Fe^{3+} ions in oxide materials. Appl. Surf. Sci. 2008; 254: 492-499.

48. Herng TS, Xiao W, Poh SM, He F, Sutarto R, et al. Achieving a high magnetization in sub-nanostructured magnetite films by spin-flipping of tetrahedral Fe^{3+} cations. Nano Research. 2015; 8: 2935-2945.

49. Li ZY, Jibran M, Sun X, Pratt A, Wang B, et al. Enhancement of the spin polarization of an Fe_3O_4(100) surface by nitric oxide adsorption. Phys. Chem. Chem. Phys. 2018; 20: 15871-15875.

50. Soares PIP, Lochte F, Echeverria C, Pereira LCJ, Coutinho JT, et al. Thermal and magnetic properties of iron oxide colloids: influence of surfactants. Nanotechnology. 2015; 26: 425704 (1pp).

51. Gaarenstroom DW, Winograd N. Initial and final state effects in the ESCA spectra of cadmium and silver oxides. J. Chem. Phys. 1977; 67: 3500-3506.
52. Cole RJ, Brooks NJ, Weightman P, Matthew JAD. Onset of d screening in alkali and alkaline earths. Phys. Rev. B 1995; 52: 2976-2982.
53. Cole RJ, Weightman P. Separating ground state and screening contributions to chemical shifts. J. Phys. Condens. Matter. 1994; 6: 5783-5790.
54. Allen GC, Tucker PM, Wild RK. High resolution LMM Auger electron spectra of some first row transition elements. Surf. Sci. 1977; 68: 469-469.
55. Tougaard S. Software for Quantitative XPS/AES of Surface Nano-structures by Analysis of the Peak Shape and Background, ver. 5.0, QUASES Tougaard ApS. 1994-2002.
56. Jablonski A, Zemek J. Overlayer thickness determination by XPS using the multiline approach. Surf. Interface Anal. 2009; 41: 193-204.
57. Gries WH. An universal predictive formula for the inelastic mean free pathlengths of x-ray photoelectrons and Auger electrons. Surf. Interface Anal. 1996; 24: 38-50.
58. Tougaard S, Yubero F. QUEELS-ε(k,ω)-REELS: Quantitative Analysis of Electron Energy Loss Spectra: Dielectric Function Determined by Reflection Electron Energy Loss Spectroscopy, ver. 3.0. 2008.
59. Tahir D, Ilvas S, Abdullah B, Armynah B, Kang HJ. Electronic properties of composite iron (II, III) oxide Fe_3O_4 carbonaceous absorber materials by electron spectroscopy. J. Electron Spectrosc. Rel. Phenom. 2008; 229: 47-51.
60. Wagner CD. Auger lines in x-ray photoelectron spectrometry. Anal. Chem. 1972; 44: 967-973.
61. Kouotou PM, El-Kasmi A, Wu LN, Wagas M, Tian ZY. Particle size-band gap energy-catalytic properties relationship of PSE-CVD-derived Fe_3O_4 thin films. Journal of the Taiwan Institute of Chemical Engineers. 2018; 93: 427-435.
62. Ganguly BN, Maity B, Maity TK, Manna J, Roy M, et al. L-cyteine-conjugated ruthenium hydrous oxide nanomaterials with anticancer active application. Langmuir. 2018; 34: 1447-1456.
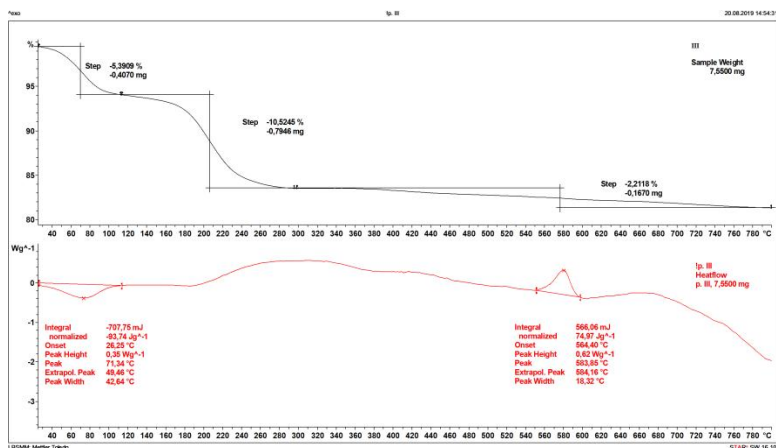
Supplementary Material
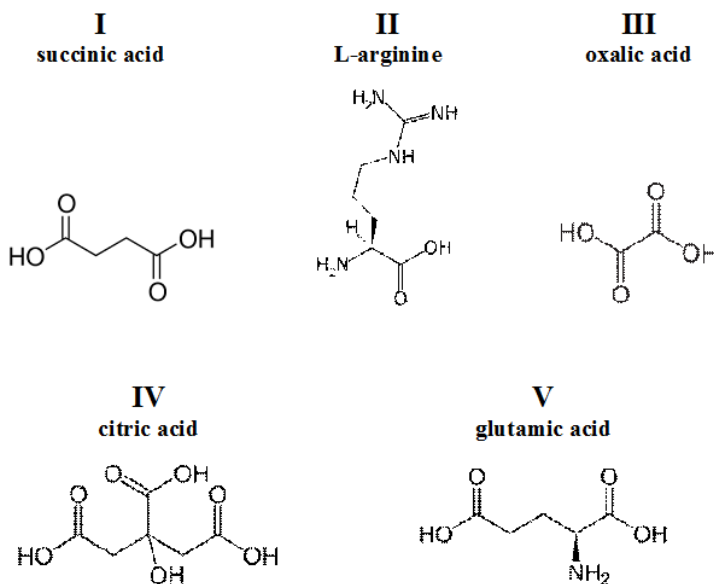
Supplementary Figure S1: Structural formulae of adsorbing molecules functionalizing the Fe_3O_4 nanoparticles.
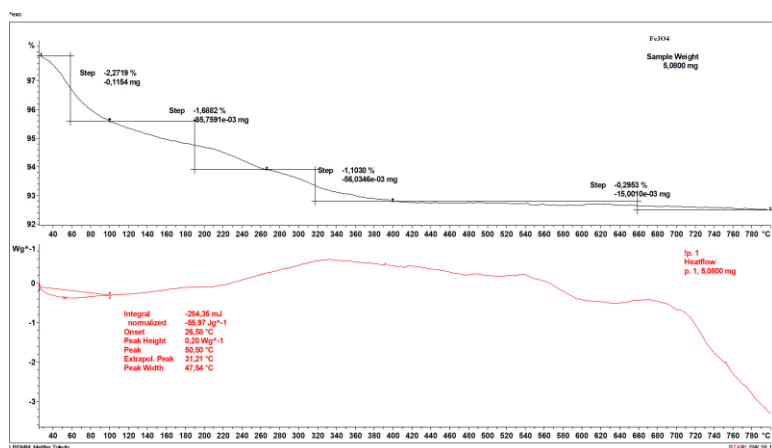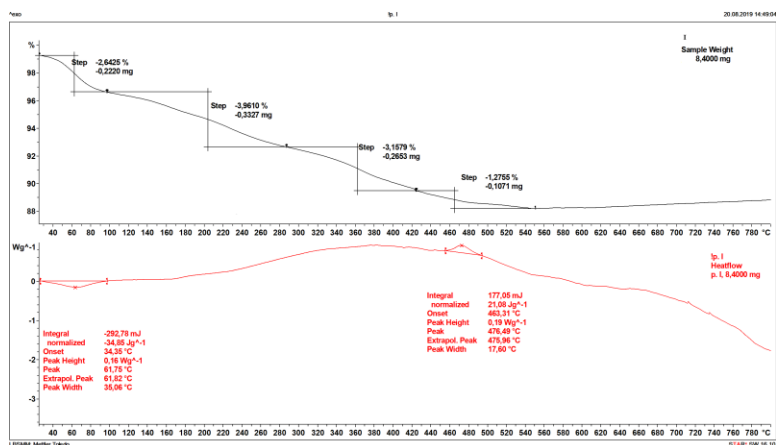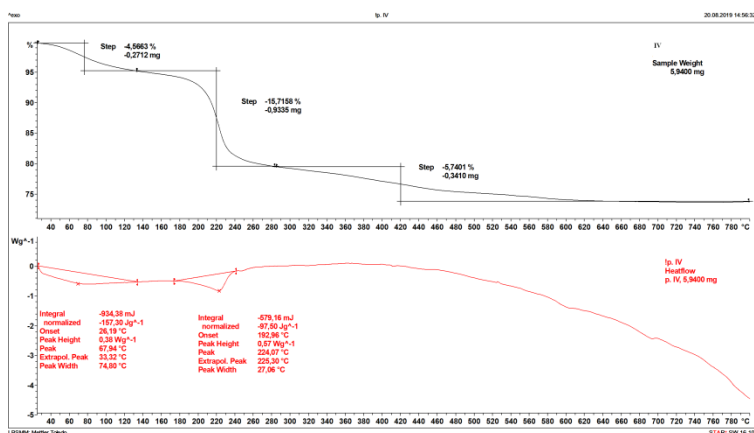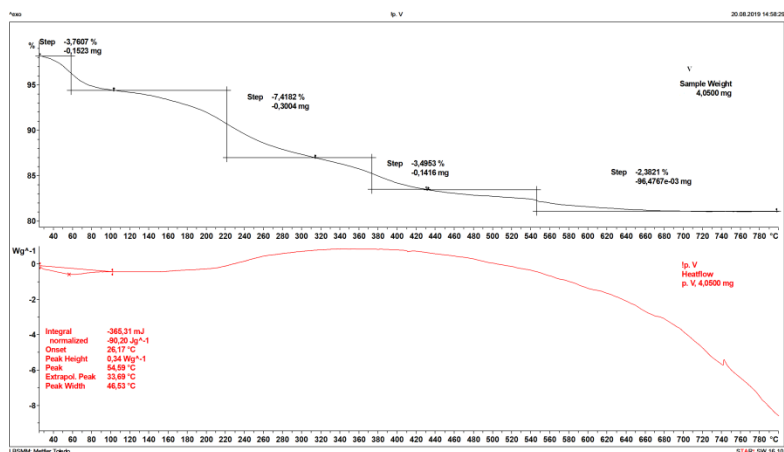
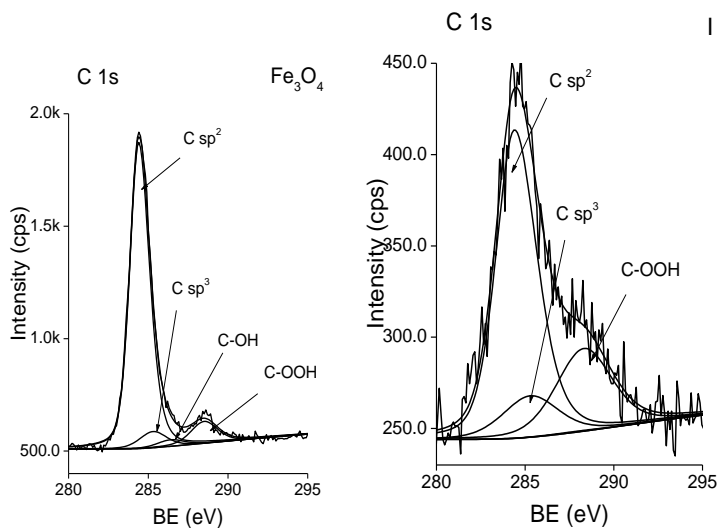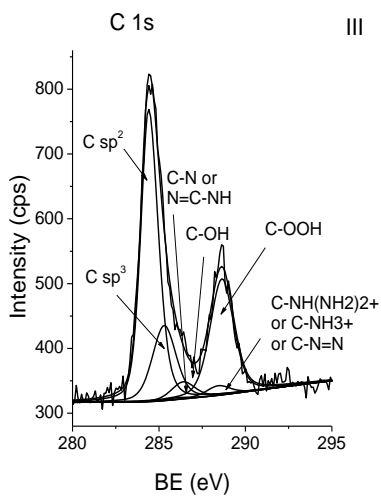**Supplementary Figure S2A:** TGA and DSC thermoanalytical curves recorded from Fe$_3$O$_4$ MNPs and Fe$_3$O$_4$ f-MNPs I.
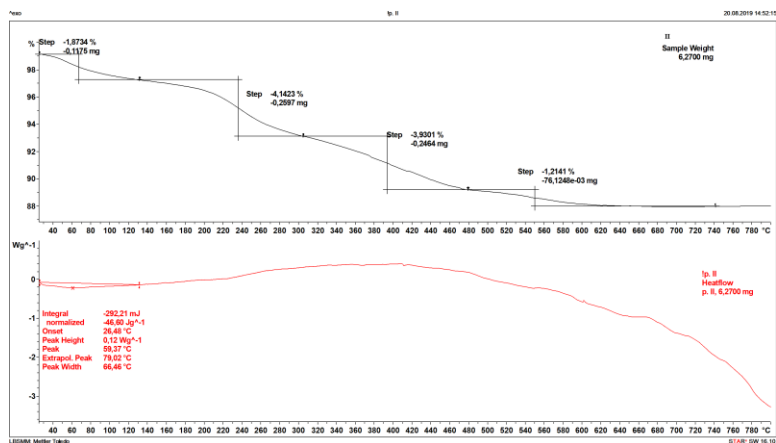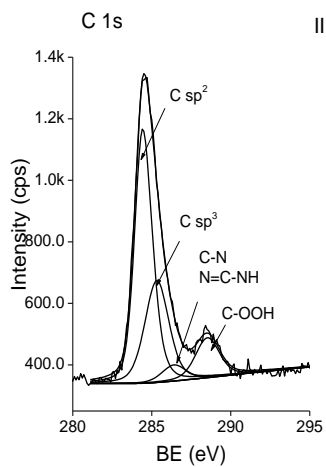
Supplementary Figure S2B: TGA and DSC thermoanalytical curves recorded from Fe_3O_4 f-MNPs II and Fe_3O_4 f-MNPs III.
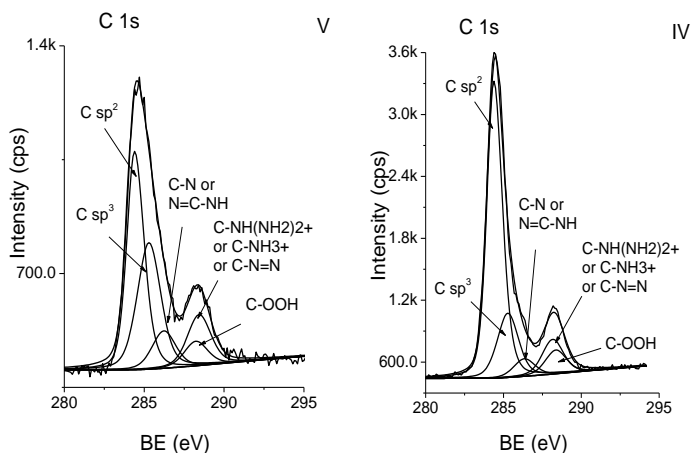
Supplementary Figure S2C: TGA and DSC thermoanalytical curves recorded from Fe_3O_4 f-MNPs IV and Fe_3O_4 f-MNPs V.

www.videleaf.com

C 1s   II

C sp^2

C sp^3

C-N
N=C-NH

C-OOH

Intensity (cps)

BE (eV)

C 1s   III

C sp^2

C-N or
N=C-NH

C-OH

C-OOH

C sp^3

C-NH(NH2)2+
or C-NH3+
or C-N=N

Intensity (cps)

BE (eV)

Supplementary Figure S3A: The XPS C 1s spectra recorded from Fe$_3$O$_4$ MNPs and Fe$_3$O$_4$ f-MNPs I-V fitted to different chemical forms.
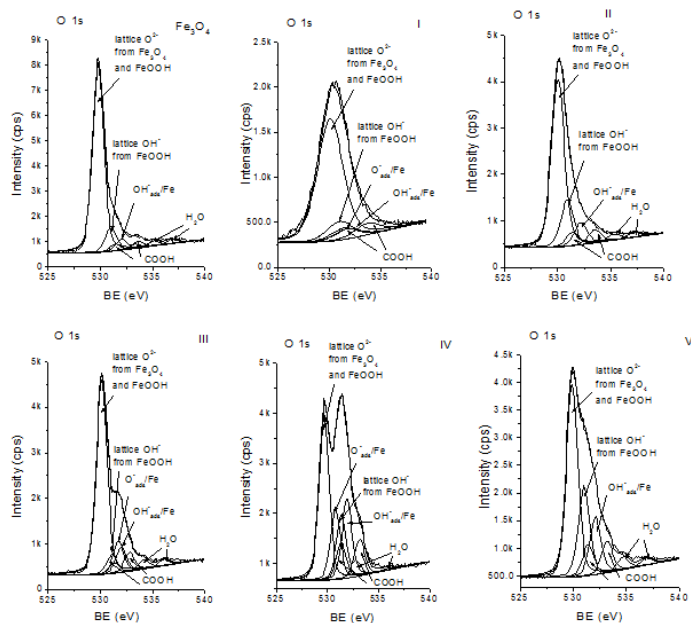
Supplementary Figure S3B: The XPS O 1s spectra recorded from Fe$_3$O$_4$ and Fe$_3$O$_4$ f-MNPs I-V fitted to different chemical forms.
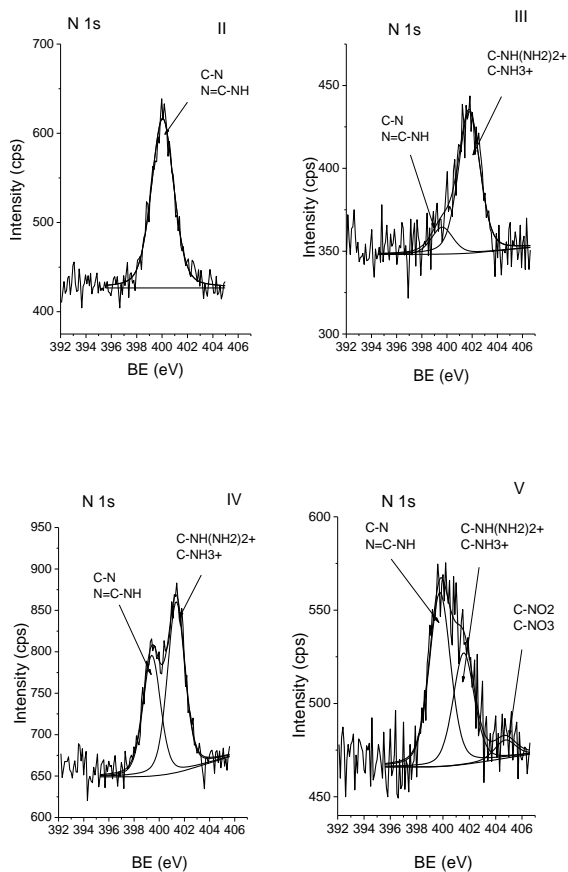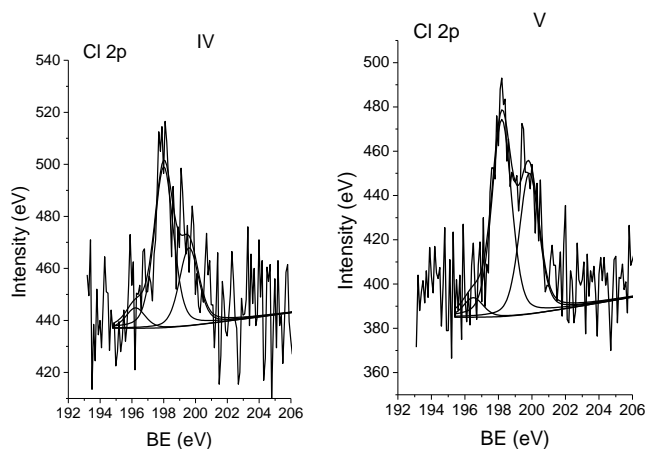
Supplementary Figure S3C: The XPS N 1s spectra recorded from samples II-V of Fe$_3$O$_4$ f-MNPs fitted to different chemical forms.
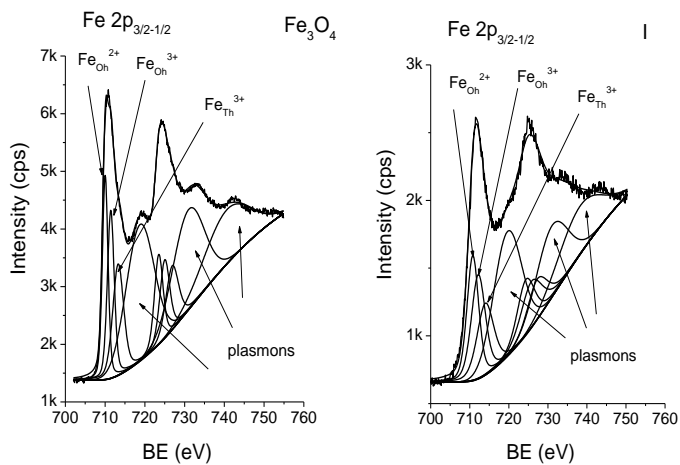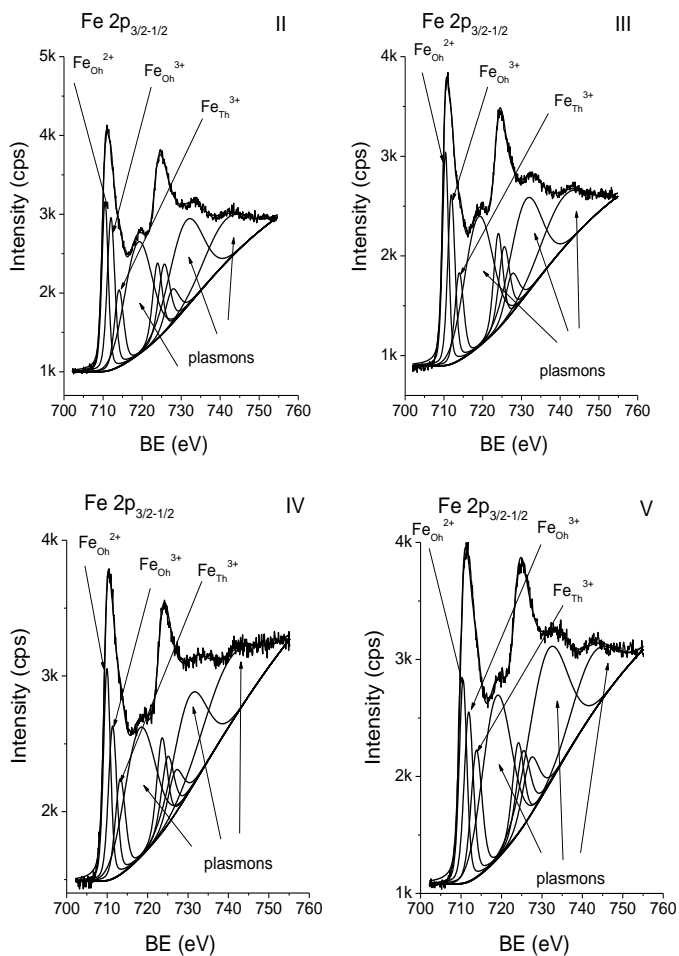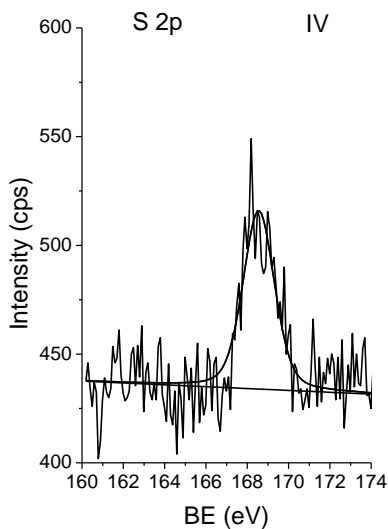
Supplementary Figure S4: The XPS Fe 2p spectra recorded from Fe_3O_4 MNPs and Fe_3O_4 f-MNPs I-V fitted to different chemical forms.
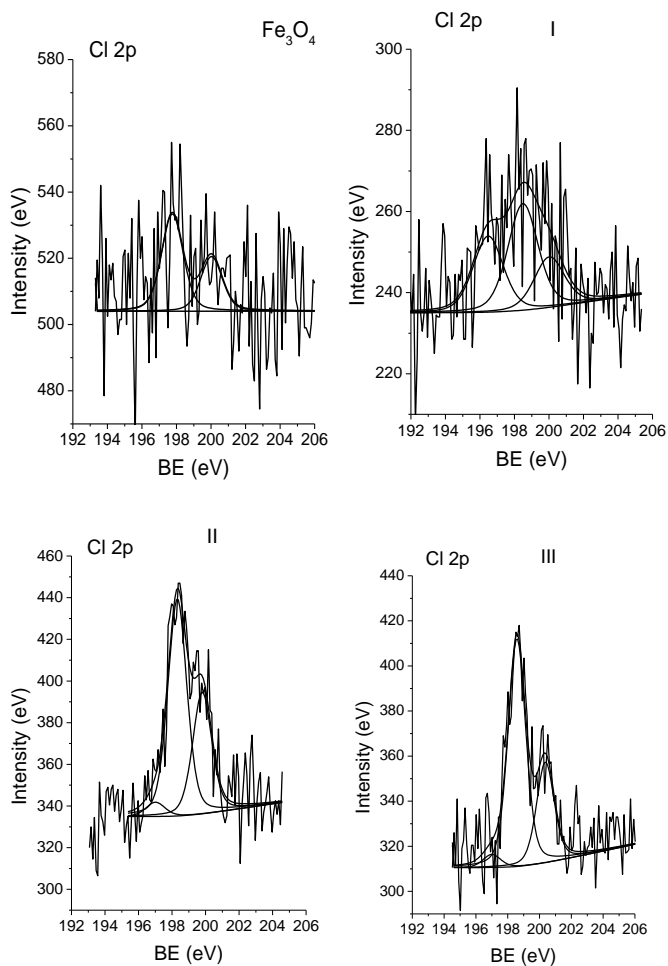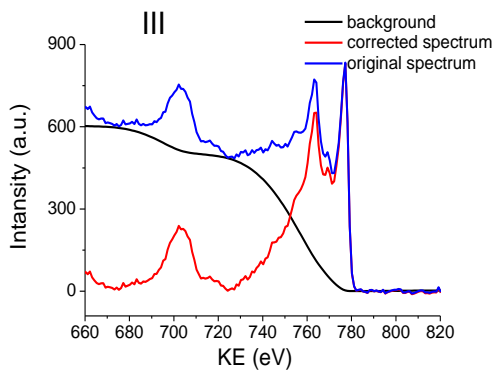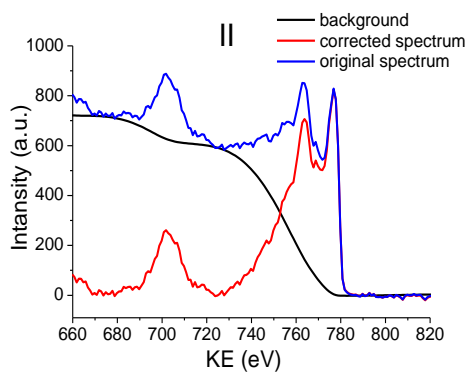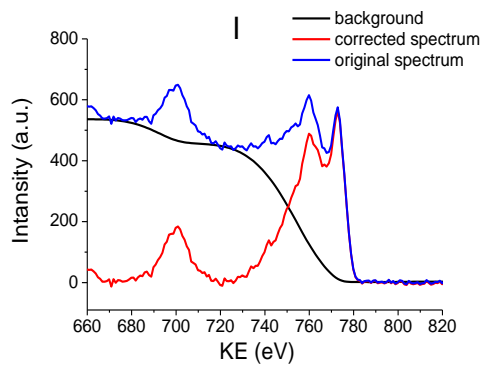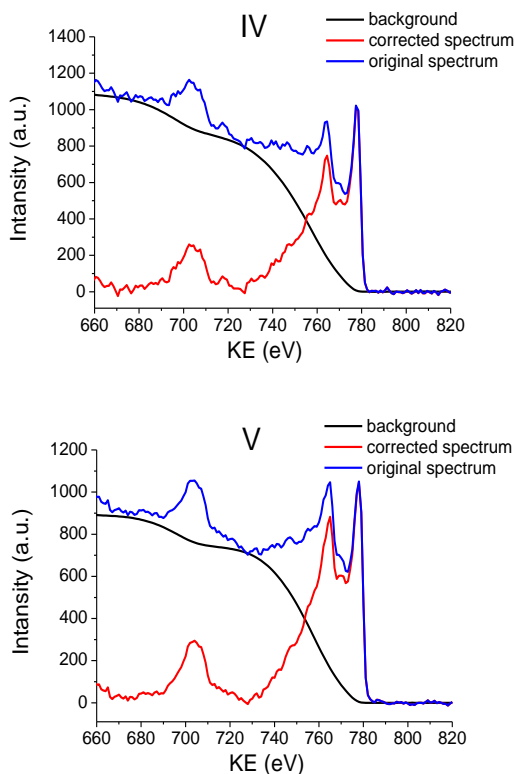
Supplementary Figure S5A: The XPS Cl 2p spectra recorded from Fe_3O_4 MNPs and Fe_3O_4 f-MNPs I-V fitted to different chemical forms.

Supplementary Figure S5B: The XPS S 2p spectrum recorded from sample IV Fe_3O_4 f-MNPs fitted to a chemical form.

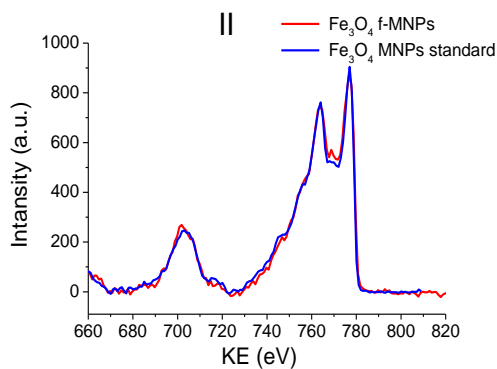**Supplementary Figure S6A :** Results of background subtraction of XPS Fe2p spectra recorded from various adsorbed molecule overlayers on Fe$_3$O$_4$ MNPs substrate (Fe$_3$O$_4$ f-MNPs I-V) using QUASES-Analyze Buried Layer (BL) without a standard.
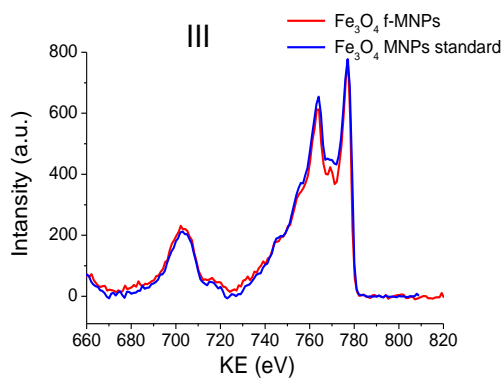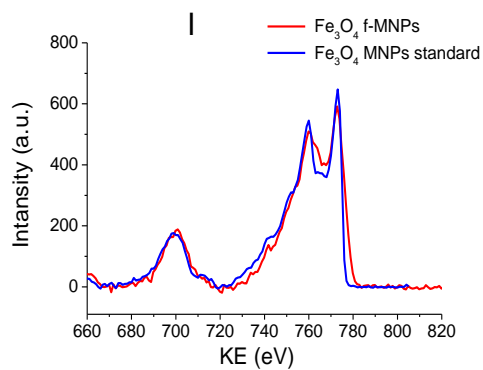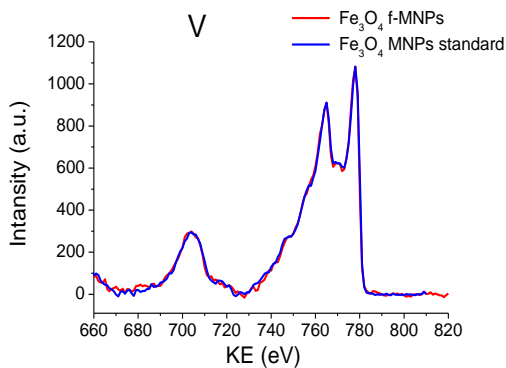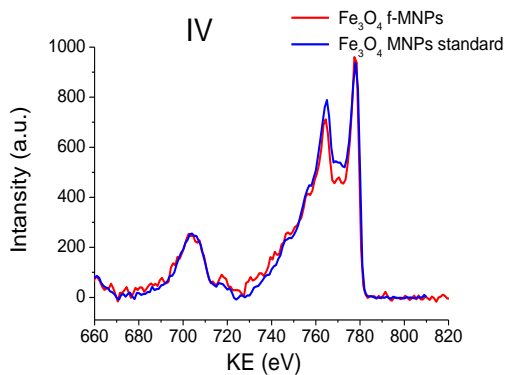
Supplementary Figure S6B : Results of adjustment of XPS Fe2p spectra recorded from various adsorbed molecule overlayers on Fe_3O_4 MNPs substrate (Fe_3O_4 f-MNPs I-V) to respective spectra recorded from Fe_3O_4 standard using QUASES-Analyze Buried Layer (BL) model.
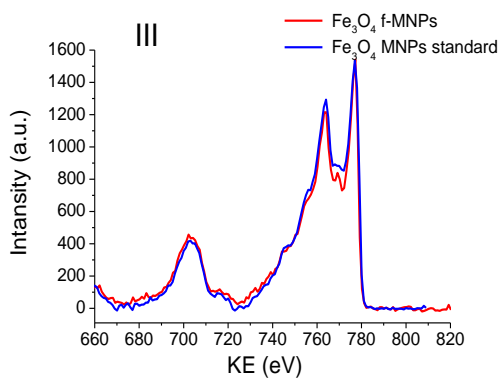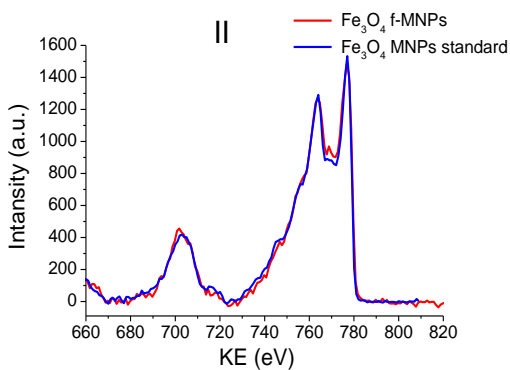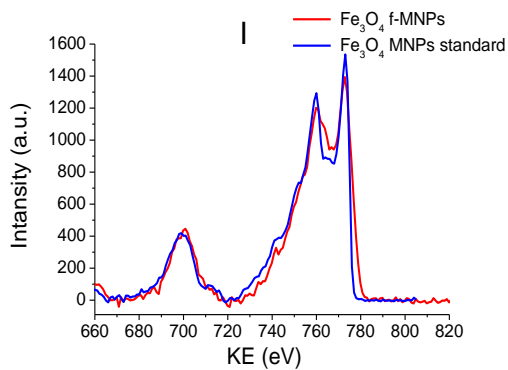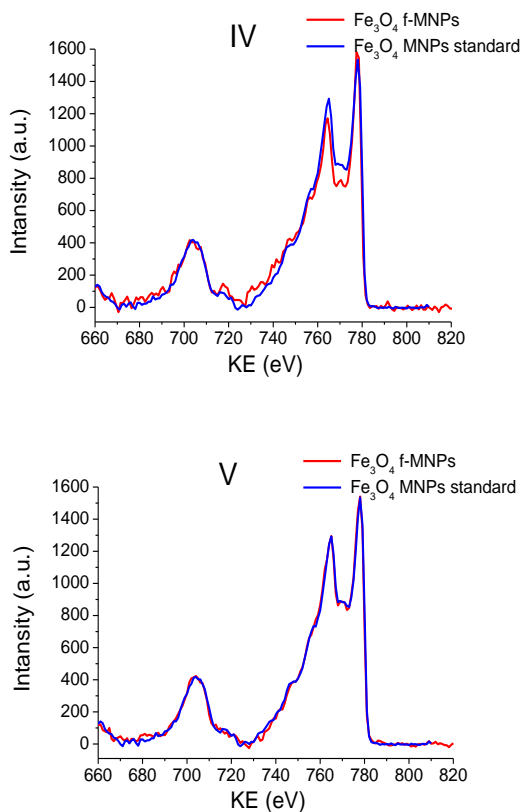
Supplementary Figure S6C : Results of adjustment of XPS Fe2p spectra recorded from various adsorbed molecule overlayers on Fe$_3$O$_4$ MNPs substrate (Fe$_3$O$_4$ f-MNPs I-V) to respective spectra recorded from Fe$_3$O$_4$ standard using QUASES-Analyze Active Substrate (AS) model.

Supplementary Table S1: XPS quantitative results for Fe_3O_4 MNPs and Fe_3O_4 f-MNPs I-V. Samples f-MNPs I-V are listed in the order of decreasing cytotoxicity.

Sample	Elemental content (atomic %)					
	C	O	N	Cl	S	Fe
Fe_3O_4	16.9	50.7	-	0.1	-	32.6
III	18.3	50.3	2.0	1.5	-	28.0
I	19.0	53.8	-	1.5	-	25.8
V	25.8	45.1	1.7	1.1	-	26.2
IV	49.4	35.1	2.4	0.4	1.1	11.6
II	22.6	45.9	2.2	1.9	-	27.3

Supplementary Table S2A: Atomic content and line positions (eV) of carbon-oxygen and carbon-nitrogen groups resulting from fitting of C 1s spectra for Fe_3O_4 MNPs and Fe_3O_4 f-MNPs I-V. Samples f-MNPs I-V are listed in the order of decreasing cytotoxicity.

Sample	C chemical states (atomic %)						
	C sp^2	C sp^3	C-OH	C=O	C-OOH	C-N N=C-NH	C-NH(NH$_2$)$_2^+$ C-NH$_3^+$ C-N=N
	BE (eV) 284.4	BE (eV) 285.3	BE (eV) 286.4	BE (eV) 287.9	BE (eV) 288.5±0.1	BE (eV) 286.3±0.2	BE (eV) 288.3±0.1
Fe_3O_4	14.3	0.9	0.4	-	1.3	-	-
III	9.4	3.0	0.7	-	4.7	0.1	0.4
I	12.6	2.1	-	-	4.3	-	-
V	10.9	7.9	-	-	3.2	2.3	1.5
IV	31.0	8.4	-	-	3.1	2.3	4.6
II	12.7	6.4	-	-	2.5	1.0	-

Supplementary Table S2B: Atomic content and line positions (eV) of oxygen chemical forms resulting from fitting of O 1s spectra for Fe_3O_4 MNPs and Fe_3O_4 f-MNPs I-V. Samples f-MNPs I-V are listed in the order of decreasing cytotoxicity.

Sample	O chemical states (atomic %)					
	Lattice O^{2-} Fe$_3$O$_4$ FeOOH	Adsorbed O$^-_{ads}$	Lattice OH$^-$ FeOOH	Adsorbed OH$^-_{ads}$	H$_2$O	C-OOH
	BE (eV) 530.0±0.2	BE (eV) 531.7±0.2	BE (eV) 531.0±0.2	BE (eV) 532.0±0.1	BE (eV) 533.0±0.2 534.8±0.5 536.6±0.5	BE (eV) 531.3±0.1 533.2±0.3
Fe_3O_4	38.2	-	4.9	2.3	0.8; 1.0 ;0.9	1.3;1.3
III	31.0	5.1	1.6	4.1	0; 1.5; 1.0	3.0;3.0
I	35.7	3.0	5.5	3.0	0; 0; 0	3.3;3.3
V	20.6	-	9.6	6.1	0; 1.4; 0.8	3.3;3.3
IV	12.4	4.8	5.3	5.9	1.2; 0.1	2.7;2.7
II	28.1	-	7.7	3.7	1.0; 0.8	2.3;2.3

Supplementary Table S2C: Atomic content and line positions (eV) of nitrogen chemical forms resulting from fitting of N 1s spectra for Fe$_3$O$_4$ MNPs and Fe$_3$O$_4$ f-MNPs I-V. Samples f-MNPs I-V are listed in the order of decreasing cytotoxicity.

Sample	N chemical states (atomic %)		
	C-N N=C-NH	C-NH(NH$_2$)$_2$$^+$ C-NH$_3$$^+$	C-NO$_2$ C-NO$_3$
	BE (eV) 399.7±0.3	BE (eV) 401.6±0.2	BE (eV) 404.7
III	0.3	1.7	-
V	1.0	0.6	0.1
IV	1.0	1.4	-
II	2.2	-	-

Supplementary Table S3:
Atomic content and line positions (eV) of chlorine chemical forms resulting from fitting of Cl 2p spectra for Fe$_3$O$_4$ MNPs and Fe$_3$O$_4$ f-MNPs I-V. Samples f-MNPs I-V are listed in the order of decreasing cytotoxicity.

Sample	Cl chemical state (atomic %)		
	[(CH$_3$)$_4$N]Cl [N(C$_2$H$_5$)4]Cl	C(NH$_2$)$_3$Cl	Met-Cl (-CH$_2$CHO(Cl)-)$_n$
	BE (eV) 196.6±0.3	BE (eV) 198.2±0.3	BE (eV) 199.9±0.3
Fe$_3$O$_4$	-	0.06	0.04
III	0.1	1.0	0.4
I	0.5	0.7	0.3
V	0.1	0.6	0.4
IV	0.1	0.2	0.1
II	0.9	1.3	0.7

Supplementary Table S4A: Parameters of Fe $L_3M_{45}M_{45}$ Auger and Fe $2p_{3/2}$ photoelectron spectra and Auger parameters for Fe_3O_4 MNPs and Fe_3O_4 f-MNPs I-V. Samples f-MNPs I-V are listed in the order of decreasing cytotoxicity.

Sample / Parameter	Fe$_3$O$_4$	III	I	V	IV	II
Fe $L_3M_{45}M_{45}$ KE (eV)	700.75	700.76	703.32	701.55	700.49	699.54
Fe $2p_{3/2}$ BE (eV)	710.78	710.97	711.39	711.15	711.16	712.11
ΔE_A $L_3M_{45}M_{45}$	0	-0.01	-2.57	-0.8	0.26	1.21
ΔE_B Fe $2p_{3/2}$	0	-0.19	-0.61	-0.37	-0.38	-1.33
β	2833.1	2833.7	2837.5	2835.0	2834.0	2835.9
α	1411.5	1411.7	1414.7	1412.7	1411.7	1411.7
Δβ	0	-0.6	-4.4	-1.9	-0.9	-2.8
Δα	0	-0.2	-3.2	-1.2	-0.2	-0.2

Supplementary Table S4B: Parameters of O KLL Auger and O 1s photoelectron spectra and Auger parameters for Fe_3O_4 MNPs and Fe_3O_4 f-MNPs I-V. Samples f-MNPs I-V are listed in the order of decreasing cytotoxicity.

Sample / Parameter	Fe$_3$O$_4$	III	I	V	IV	II
O KLL KE (eV)	512.68	511.81	514.28	512.59	511.54	511.55
O 1s BE (eV)	529.98	529.97	530.39	530.15	531.20	530.15
ΔE_A O KLL	0	0.9	-1.6	0.1	1.1	1.1
ΔE_B O 1s	0	0	-0.4	-0.2	-1.2	-0.2
β	2102.6	2101.7	2105.5	2103.0	2105.1	2102.0
α	1042.7	1041.8	1044.7	1042.7	1042.7	1041.7
Δβ	0	0.9	-2.9	-0.4	-2.5	0.6
Δα	0	0.9	-2.0	0	0	1